nature physics

Article

https://doi.org/10.1038/s41567-025-02825-9

Enzymes as viscoelastic catalytic machines

Received: 21 May 2023

Accepted: 12 February 2025

Check for updates

Eyal Weinreb[1,15], John M. McBride[2,15], Marta Siek[3], Jacques Rougemont[4], Renaud Renault[5], Yoav Peleg[6], Tamar Unger[6], Shira Albeck[6], Yael Fridmann-Sirkis[7], Sofya Lushchekina[8], Joel L. Sussman[9], Bartosz A. Grzybowski[3,10,11], Giovanni Zocchi[12], Jean-Pierre Eckmann[4,13], Elisha Moses[1] ✉ & Tsvi Tlusty[2,14] ✉

The catalytic cycle involves internal motions and conformational changes that allow enzymes to specifically bind to substrates, reach the transition state and release the product. Such mechanical interactions and motions are often long ranged so that mutations of residues far from the active site can modulate the enzymatic cycle. In particular, regions that undergo high strain during the cycle give mechanical flexibility to the protein, which is crucial for protein motion. Here we directly probe the connection between strain, flexibility and functionality, and we quantify how distant high-strain residues modulate the catalytic function via long-ranged force transduction. We measure the rheological and catalytic properties of wild-type guanylate kinase and of its mutants with a single amino acid replacement in low-/high-strain regions and in binding/non-binding regions. The rheological response of the protein to an applied oscillating force fits a continuum model of a viscoelastic material whose mechanical properties are significantly affected by mutations in high-strain regions, as opposed to mutations in control regions. Furthermore, catalytic activity assays show that mutations in high-strain or binding regions tend to reduce activity, whereas mutations in low-strain, non-binding regions are neutral. These findings suggest that enzymes act as viscoelastic catalytic machines with sequence-encoded mechanical specifications.

Protein function is the end-product of collective interactions that emerge from the particular sequence of amino acids encoded in the gene. In enzymes, evolutionary processes have fine-tuned the active-site geometry and composition[1–10] such that the preorganized catalytic groups can stabilize the transition state[11–16] and, consequently, accelerate reactions by many orders of magnitude[17,18]. However, beyond the local scale of the active site, the function of enzymes also relies on the evolution of multiscale motions that occur over the entire protein during the catalytic cycle[19–26], even in regions distant from the active site[27–33]. These internal motions and rearrangements of amino acids facilitate substrate binding and alignment (apo to holo transformation) and product release[34–37], and underlie the basic biochemical mechanisms such as induced fit[38–40], conformational selection[41], conformational proofreading[42–44] and allostery[45–49]. The flexibility of enzymes also affects the chemical steps[50–53], and the influence of mutations may be long ranged[29–31], although the motions involved are typically smaller.

Since dynamics and conformational changes are central to the function of many proteins, it is natural to investigate their mechanical properties within the physical frameworks developed to study viscoelastic matter[54] and amorphous solids[55]. Furthermore, these functional motions of the protein are often long-ranged 'soft modes'[56–61], which spread over many atoms and residues and depend on the global structure and surface patterns of the protein[62–65]. We, therefore, propose and demonstrate in this paper that the large-scale dynamics of the protein can be adequately treated within the continuum theory usually applied

A full list of affiliations appears at the end of the paper. ✉e-mail: elisha.moses@weizmann.ac.il; tsvitlusty@gmail.com

to model macroscopic objects. This requires special caution since, at the nanometric scale of proteins, thermal fluctuations are much more significant and should be appropriately averaged.

In examining how evolution shapes the mechanical properties of enzymes, we aim to probe and estimate the subtle displacements and rearrangement of amino acids that occur during conformational changes[33,66–68]. In particular, protein function relies on the existence of flexible regions that enable conformational changes and internal shearing, twisting and pivoting motions, such as in hinges[45,47,48,69–73]. A natural measure for such changes is the strain[62,64,66], which probes the mechanical stresses and deformations propagating through the protein[19,49,57,58,68,74–76]. In continuum mechanics, one calculates the strain by measuring the displacement of the material with respect to a reference state and then taking a spatial derivative of the displacement, which yields the strain tensor[77]. When the displacement is spatially uniform, the strain vanishes, whereas high strain indicates variation in the displacement, that is, local deformation. Strain can also be computed at the atomic level, in ordered crystals or amorphous matter such as proteins[57,58,62,64,66,68,74,78]. The discrete, atomistic analogue of the spatial derivative is the relative change in distances between neighbouring atoms and amino acids, from which we derive the effective strain[62,64] (Methods).

The internal response to externally induced strain in proteins has recently been shown to be viscoelastic, that is, to include motion that is both spring-like and friction dominated[79–82]. The elastic response of the protein originates from bonds being stretched, compressed or twisted under the influence of forces. The resulting spring-like motion is atomistically understood by analysing the vibration spectrum of the protein, experimentally by infrared/Raman measurements, computationally by molecular dynamics (MD) simulations[1,21,83,84] and by normal mode analysis[25,58,68,74,85,86]. During the motion of the protein, bonds can break and reform, and new bonds can be created. Such plastic deformation induces 'internal friction' and effective viscous forces. In this paper, we link the atomistic measures of elasticity and viscosity to their coarse-grained continuum description and show that at the large scale, the effect of mutation can be accounted for as a variation in the effective continuum parameters, especially the spring constant[34] and viscosity[79].

As is often the case with emergent properties[87], it is difficult to evaluate or measure the contribution of a single amino acid to the collective motion of a protein. Computationally, one may estimate the strain involved in functional motion by comparing how much each amino acid moves relative to its neighbouring residues between unbound and bound static conformations[57,62,66]. It has been theoretically proposed that mutations in high-strain regions would have a significant effect on function[57,58,68]. Yet, the degree to which a single amino acid replacement in a critical area can actually affect activity—not only by changing the chemical binding to substrate molecules and their transition states but also by modifying the large-scale mechanical properties of the protein[88]—remains an open and important question[89–92].

Our hypothesis is that regions that experience high strain during the catalytic cycle give the protein mechanical flexibility crucial for protein motion during functionality[57,58,68]. Strain can, therefore, serve as a predictive tool for functionally relevant viscoelastic protein properties. A key obstacle in demonstrating this stems from the difficulty of measuring and analysing minute forces and displacements in the sub-nanometre regime. Therefore, to gain an insight into the internal viscoelastic dynamics of enzymes and their functional role, here we utilize two technological advances—the nano-rheological viscoelasticity measurement[81] and DeepMind's AlphaFold2 (AF) software[93].

Using these tools, we focus on the guanylate kinase enzyme[94,95] (from *Mycobacterium tuberculosis*), which is part of a large family of enzymes that undergo conformational changes as part of their function[19,38,39,45,50,71,83,96,97]. We test several theoretical ideas by measuring and linking the mechanical, structural and functional effects of single amino acid replacement mutants (Fig. 1a). In particular, we ask whether and how mutating high-strain amino acids affects the enzyme's flexibility and dynamics compared with mutating low-strain amino acids, and whether it may also impact activity.

To test our hypothesis, we prepared 34 mutants with a single amino acid substitution (Methods). The amino acids chosen as substitutes were selected to have relatively similar physicochemical characteristics, as estimated by their BLOSUM62 scores. Most substitutions have non-negative scores, implying that, on average, they are relatively common replacements among similar proteins.

To select the positions of amino acid substitutions, we use two complementary computational methods, allowing us to prelocate mechanically relevant residues. We first calculate the effective strain from the conformational change due to binding by comparing the apo (that is, unbound) and holo (that is, bound) forms of wild-type (WT) guanylate kinase in the Protein Data Bank (PDB)[98], from which we identify high-strain regions in which deformation is substantial[68]. This is the binding strain, which, unless otherwise stated, is the one that we use throughout this paper to estimate the effective strain.

Independently, we utilize AF to quantify the local structural change resulting from a point mutation. We compare the apo structures predicted by AF for the unmutated and mutated enzymes, and measure the effective strain, that is, the mean relative change in atomic distances between neighbours, caused by the single amino acid replacement[62,64]. This 'mutation strain' is an independent, sensitive probe for local amino acid rearrangement in the equilibrium structure induced by mutations. Note that strain measures deformation that can result either from physical or evolutionary processes: the physical strain is the response to physical stresses, whereas the mutation strain reflects the modulation of energy landscapes that results in a redistribution of protein conformations in the equilibrium ensemble[58,99].

Next, we divide mutants of guanylate kinase into two groups according to their strain: those that are expected to be approximately 'as flexible as before' (the control group of residues with strain below the given threshold; Methods) versus those expected to exhibit 'changed flexibility' (the high-strain group, with strain above the threshold). As a positive control for direct effects on the active site, we add a third group of residues involved in binding (the binding group). We rely on experiments to verify that both enzymatic activity and a direct measure of viscoelastic motion bear out this division into groups.

Specifically, we hypothesize the following: (1) mutants from the high-strain group will tend to hinder both viscoelastic motion and enzymatic activity; (2) the mutations in low-strain, non-binding locations will have minimal effects on viscoelasticity and activity. We have no a priori expectations about the effect of mutations in the binding sites on viscoelasticity.

We then apply the nano-rheology method (Fig. 1b) to measure the viscoelastic response to externally applied periodic mechanical perturbation in a subset of nine mutants across the three groups. This method measures the internal motion of the protein when stretched and compressed at biologically relevant driving frequencies of 5–120 Hz, which correspond to the large-scale slow motions of the protein[81]. The method relies on a response signal that is locked to the perturbation, and is averaged over 10^6–10^9 molecules, strongly suppressing thermal and other noise sources. This approach enables sub-ångström resolution for the resultant change in the protein extent along the stretching/compression axis.

By observing the phase shift between the perturbation and response (that is, the phase between the applied electric field and the periodic motion of the charged gold nanoparticle attached to the protein molecule, as a function of the frequency), we model and confirm theoretical insights for the viscoelastic effect of mutations in the three examined regions of the enzyme. The guanylate kinase protein is shown to respond as a viscoelastic material, with particular contributions stemming from the relaxation of prestressed[55,100] amino acid bonds when force is applied.

https://doi.org/10.1038/s41567-025-02825-9

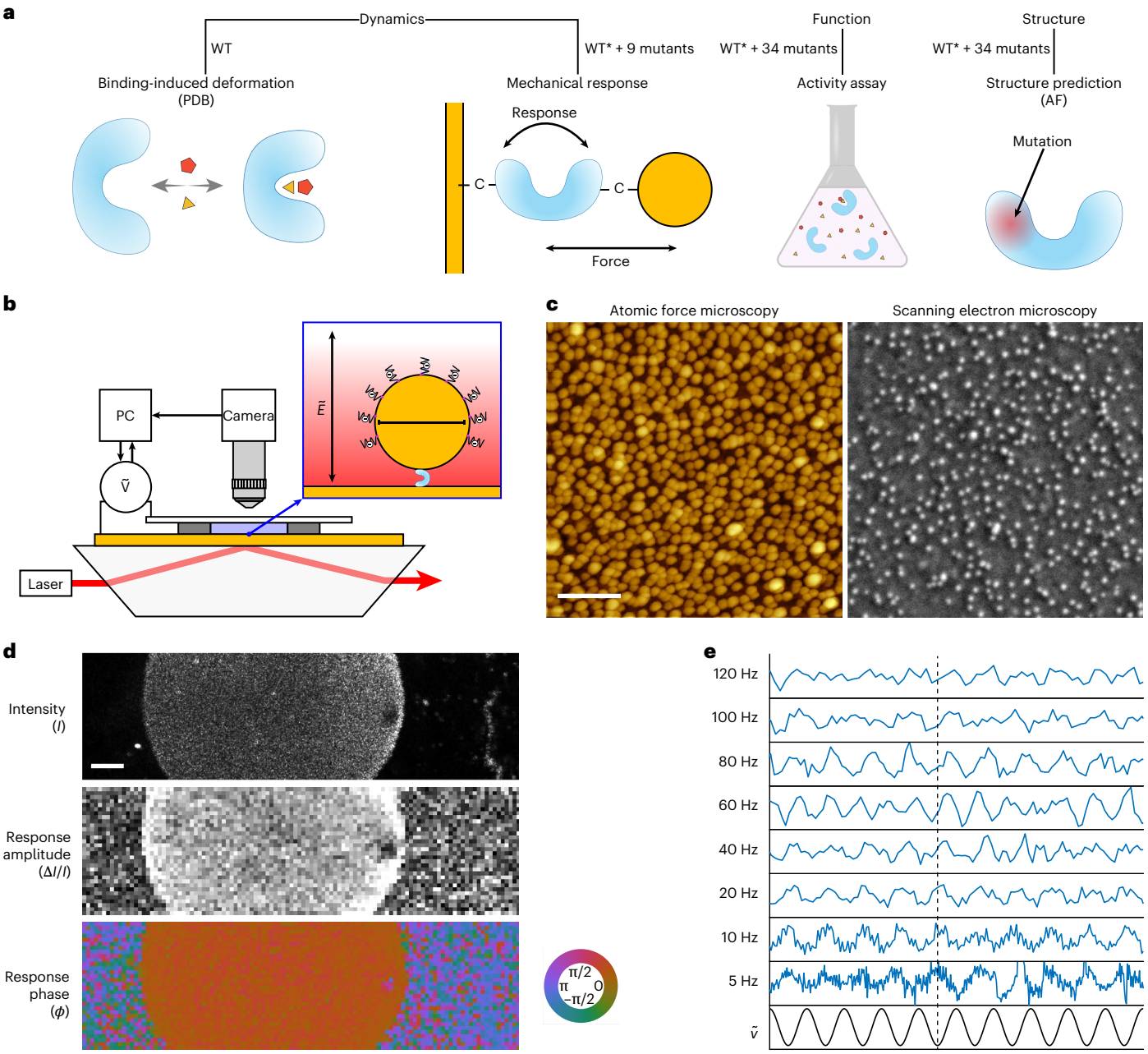

Fig. 1 | Schematic and details of experiment. a, Schematic: probing the mechanics of guanylate kinase, through dynamics, activity and structure. Left: apo form of WT has an open structure[98] and deforms on binding into the holo form[94]. Using this deformation, we locate high-strain regions, hypothesized to be important for mechanics. We measure the mechanical response to the applied oscillating force for a cysteine-substituted variant WT* and nine mutants in the 'high-strain', 'binding' and 'control' groups. Middle: enzymatic activity assessed for WT* and 34 mutants. Right: protein structure is predicted using AF for WT* and 34 mutants to estimate the effect of mutations on structure. **b**–**e**, Nano-rheology. **b**, Enzymes attached to a gold-coated glass slide, and on the other side, to a gold nanosphere bead covered with negatively charged single-strand DNA. A Dove prism creates an evanescent light field (red), emanating from the gold surface, falling off quickly with depth as the beads are illuminated, causing changes in the beads' vertical position to induce changes in the intensity of light that the beads scatter. Alternating electric potential applied to the top and bottom of the sample induces electric forces, pulling the beads up and down (opposite to the voltage because of the negative charge). This stretches and compresses the proteins at the frequency of alternation. The resulting scattered light fluctuations were collected via a microscope, and analysed using the applied potential using a lock-in method. PC, personal computer. **c**, Atomic force microscopy and scanning electron microscopy images of the slide surface with enzyme-attached nanospheres for different samples. Scale bar, 200 nm. **d**, Example analysis images. Top: mean intensity (I) over the entire acquisition. Middle: response oscillations that are amplitude normalized by the mean intensity ($\Delta I/I$). Bottom: phase difference (ϕ) between the response oscillations and applied potential. The middle and bottom images in this example are spatially averaged over 8 × 8 pixel blocks before the lock-in analysis. Potential applied at $\omega = 20$ Hz in this case. Scale bar, 200 µm. **e**, Example $\Delta I/I$ for a single sample at all the applied frequencies. For each frequency, time is normalized by the stimulation rate, represented by the bottom trace showing the applied potential. The dashed line is a guide for the eye, representing the shift in phase over frequency.

https://doi.org/10.1038/s41567-025-02825-9

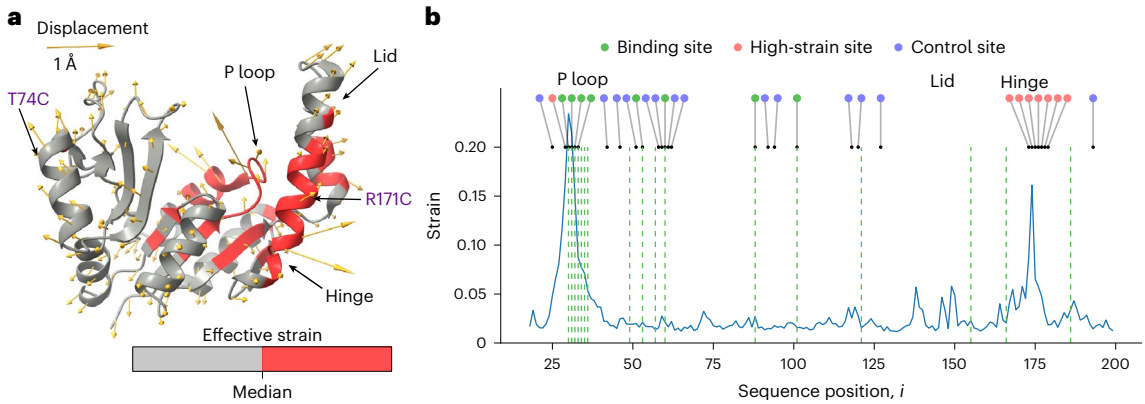

Fig. 2 | Strain computation and selection of mutants. a, Apo (1ZNW, *M. tuberculosis*)[98] guanylate kinase has an open structure; residues are coloured according to the strain caused by deformation on binding, calculated using the apo and holo (GDP-bound) forms of guanylate kinase (Methods). Displacement due to GDP binding (1ZNZ) is shown by the yellow arrows; the arrows are enlarged for visibility, and the 1-Å scale is indicated. The hinge, lid and P-loop regions are approximately indicated. The locations of two cysteine substitutions (from WT to WT*) are highlighted in purple. **b**, Strain due to GDP binding. The green dashed lines indicate residues that form hydrogen bonds with a substrate or co-factor[95]. The locations of mutation sites are shown as black circles, with groups indicated by colour. The hinge, lid and P-loop regions are approximately indicated. The strain threshold delineating the high-strain and control groups is 0.04.

Finally, the enzymatic activity of all 34 mutants is measured using a fluorometric assay. Expectedly, we find that the largest disruption of activity is caused by mutations in the binding region. A more remarkable result is that mutations in the high-strain regions have a more pronounced effect on activity than mutations in the control regions of the protein. Furthermore, we find a correlation of both mutation strain and binding strain with a reduction in enzymatic activity.

Several previous studies have substantiated that point mutations to residues far from the binding site may affect catalysis[29–31,50–53]. The present results provide the first direct experimental confirmation that such distal point mutations can also simultaneously and significantly alter the viscoelastic properties of an enzyme, and that the location of these pivotal residues can be predicted by theory. Thus, enzymes appear as deformable catalytic machines whose multiscale motions are governed by mechanical specifications encoded in the gene[19,68,87].

Results

Evaluating the strain caused by binding in guanylate kinase

Binding of WT guanylate kinase to adenosine diphosphate (ADP) and guanosine monophosphate (GMP) is associated with a large-scale conformational change (Fig. 1a and Supplementary Video 1)[98], where an intertwined pair of α-helices (the lid region) collectively moves to cover the bound substrates (Extended Data Fig. 1a)[94]. This kind of global motion—essential to the function of many enzymes[27,28,36,46,50,51,66,78,101,102]—was theoretically proposed to arise through evolution to facilitate low-energy, large-scale conformational change[57,58,68]. This motion typically generates regions of high strain (Methods), where a substantial local rearrangement of the structure occurs[66]. The effective strain measure we use (Methods) estimates the average relative change in distances due to this rearrangement[62]. We find three regions with high strain (Fig. 2): the lid region, a P-loop (a conserved phosphate-binding motif)[103] and a region at the base of the lid that appears to act as a hinge-like pivot. We hypothesize that these high-strain residues are essential to the large-scale motion of the protein and, therefore, to its function.

Mutations in binding and non-binding regions

We chose 34 guanylate kinase mutants to cover a wide range of strains and distances from the binding sites. To choose mutations that are involved in binding, we took those residues that were found in silico to be in contact with one of the substrates or a metallic co-factor[95]. This group is labelled binding, and includes residues that are directly involved in the catalytic process[4]. Our model hypothesizes that residues that are far from the binding site will be important for binding only if they are in a high-strain region. To test this hypothesis, we chose to mutate high-strain residues that are mainly further from the binding site; these mutants are labelled as high strain. The remaining mutations, which are not involved in binding and have a low strain, are labelled control.

Nano-rheology

We applied an oscillating electrical potential at frequencies ranging from 5 Hz to 120 Hz to drive the motion of enzyme-tethered beads (Fig. 1b–e and Methods), and Fig. 3 shows the phase difference (ϕ) and amplitude ($\Delta I/I$) of the generated oscillations in the light scattered by the beads. We performed these experiments on a cysteine-substituted variant of the WT enzyme (WT*; Extended Data Fig. 2) and nine mutants (four from the high-strain group, three from the binding group and two from the control group, where all of them contained the same cysteine substitutions). We first examine the phase of the response because it is a more robust measurement (Methods) and can be more reliably averaged across samples and mutants. The phase difference was measured relative to the phase of the applied electrical potential. As shown in Fig. 3a, there is a clear and strong dependence of the phase difference on the frequency of the applied potential, increasing from near 0° at 0 Hz and climbing towards saturation of 90° (and somewhat beyond) at 120 Hz.

The phase measurements (Fig. 3a) show a clear separation between the high-strain group and the other two groups, with the high-strain group deviating towards larger phase shifts across the full range of frequencies ω measured. Note, however, that the three groups converge to 0° at the lowest frequencies ($\omega < 10$ Hz). The curves approximately take the shape of a simple second-degree polynomial $\phi = a\omega + b\omega^2$. Using the extra-sum-of-squares F-test, we find that the curve describing the high-strain group significantly differs from the curves of the control ($P < 10^{-4}$) and binding ($P < 10^{-6}$) groups, whereas the curves of the binding and control groups are statistically similar ($P = 0.12$).

Figure 3c shows the amplitude of the beads' traversed distances, again averaged per mutant group. The separation of the high-strain group is clear, although with high error estimates. Here lower amplitudes are indicative of a stiffer, more viscous response for mutations in the high-strain region.

In these analyses, WT* was included within the control group. Figure 3b shows a breakdown of the phase response for the individual mutants within that group. Evidently, the phase response of the WT is similar to that of the other mutants in the group.

Fits to the viscoelastic model

We fit the mechanical response to a simple physical model that describes the protein as a viscoelastic material. Figure 3d shows a scheme of the model. The motion of the bead in response to the applied voltage, Δz, originates in a spring-like release of the frustration stress[55], along with the elastic and viscous components that contribute in parallel.

As explained in the Methods, we fit the vectorially averaged amplitude $r = \Delta I/I$ and phase ϕ to circles (Fig. 3e). Despite a larger uncertainty in the amplitude data (Methods), we obtain good circle fits to the model for the three groups. The extracted model parameters for the three different mutant groups are $\omega_1 = \kappa_1/2\pi\gamma = (56 \pm 4)$ Hz, (64 ± 4) Hz and (46 ± 5) Hz and $\omega_2 = \kappa_2/2\pi\gamma = (170 \pm 11)$ Hz, (183 ± 9) Hz and (111 ± 8) Hz for the control, binding and high-strain groups, respectively (95% confidence interval). It is reassuring to note that ω_1 and ω_2 are comparable to the reported catalytic rate of guanylate kinase ($k_{cat} = 23$ Hz)[98]. We see that the turnover rate (k_{cat}) of the enzyme is located around the frequency ω_1 at which the elastic and viscous forces become comparable, and beyond which the resistance increases steeply. Thus, the working point of the protein may be optimized to be at as high a frequency as possible without incurring a prohibitive frictional cost that would hinder the motion. These ω_1 and ω_2 values also adequately describe the phase-only data (Supplementary Fig. 1).

To evaluate f/γ, we use $\delta = 100$ nm, a reasonable estimate for the characteristic evanescence length δ in our geometry. This puts the total deformation of the protein at about 1 Å, and gives a characteristic velocity $f/\gamma = (92 \pm 8)$ nm s^{-1}, (100 ± 8) nm s^{-1} and (58 ± 7) nm s^{-1} for the control, binding and high-strain groups, respectively (95% confidence interval). The resulting fit parameters of the circles are depicted as a bar graph in Fig. 3f.

From the viscoelastic model, we can evaluate the effect of the high-strain mutations on the model parameters. Such estimates are intended as an order-of-magnitude indication and the effects we look at are relative ones, that is, the ones in which we can show that the high-strain group is, on average, stiffer than the binding and control groups. Taking ratios, we eliminate f and evaluate the effective viscosity γ^{hs}, the spring constant κ_1^{hs} and the prestress constant κ_2^{hs} of the high-strain group in terms of the corresponding WT values γ^{wt}, κ_1^{wt} and κ_2^{wt}. We obtain $\gamma^{hs}/\gamma^{wt} = (1.6 \pm 0.2)$, $\kappa_1^{hs}/\kappa_1^{wt} = (1.2 \pm 0.1)$ and $\kappa_2^{hs}/\kappa_2^{wt} = (1.5 \pm 0.1)$, where the WT values are from the whole control group (± indicates the standard error). One clearly sees systematic stiffening and increased viscosity in the high-strain mutants.

To obtain rough order-of-magnitude estimates of the viscoelastic parameters, we assume a typical spring constant of protein $\kappa_1 \approx 10^2$ pN nm^{-1} (refs. 34,104), yielding a friction coefficient of $\gamma \approx 0.1$ pN s nm^{-1} for a frequency of $\omega_1 \approx 10^2$ Hz. This measure of internal friction reflects the forces involved in amino acid rearrangement during the catalytic cycles, which account for deformation, bond breaking and reformation, and local reconfiguration processes. Similar estimates of γ were obtained in previous guanylate kinase nano-rheology studies[79,81] and atomic force microscopy measurements of lysozyme[105], and are much larger than the internal friction observed during folding[106–109]. The internal friction γ is also much larger than the Stokes friction coefficient of the gold nanoparticle in water, that is, $\gamma_{hyd} \approx 10^{-7}$ pN s nm^{-1}. Therefore, hydrodynamic drag forces can be safely neglected. Although such calculations can only give ballpark estimates, from the measured characteristic f/γ, we find that the force is substantial, $f \approx 10$ pN, but weaker than the typical forces exerted to unfold proteins[110–112].

Viscoelasticity in MD simulations

We performed MD simulations on WT*, E173N (high-strain group) and G62S (control group) variants to corroborate and understand the effect of mutations on dynamics. However, we were constrained by the fact that the typical timescales available in MD simulations are considerably shorter than those implicated in protein activity and the corresponding material properties of elasticity and viscosity. Thus, Supplementary Fig. 2 shows an analysis of the root-mean-square fluctuations over 1 µs, which showed practically no difference in large-scale dynamics between the variants in equilibrium simulations. Slightly clearer differences between variants were obtained using a longer simulation time (3 µs) with the normal mode (Supplementary Fig. 3) and network community (Supplementary Fig. 4) analyses.

To overcome this disparity in timescales, we used non-equilibrium simulations in which a constant force was applied to the two cysteine residues (C75 and C171), pulling them apart. This most closely mimics the rheological experiment in which a time-oscillating force was applied to the cysteine residues. We find clear differences in the response to force in the high-strain variant, whereas the control is very similar to the WT protein (Fig. 4a). From the linear part ($F > 0$ pN) of this force–distance curve, we can estimate an effective spring constant for each protein, fitting to a purely elastic model. This measurement for the E173N variant ($\kappa = 240$ pN nm^{-1}) is about 30% stiffer than WT* ($\kappa = 180$ pN nm^{-1}) and about 15% stiffer than G62S ($\kappa = 210$ pN nm^{-1}), consistent with the rheology experiments. Errors on the fits are between 10% and 20%. We also note that the spring constants calculated from the MD simulations are in the same order of magnitude of our earlier estimate of $\kappa_1 \approx 10^2$ pN nm^{-1}.

Another way to overcome the problem of long timescales associated with energy barrier crossings is the accelerated weight histogram method (Methods). The resulting potential of mean force (PMF) curves is shown in Extended Data Fig. 4. The effective spring constants that can be estimated from the curvature are consistent with the results shown in Fig. 4a.

The rheology experiments also indicate that the high-strain variants are more viscous than the WT ones. In a given material, motion is viscous when bonds are not easily broken. In the context of the protein, we compare the number of hydrogen bonds that are created and lost. We find that compared with the WT and control variants, the high-strain variant has a concurrent lower rate of hydrogen-bond formation and breakage (Fig. 4b). Overall, these MD simulations support the findings from the rheology experiment and indicate that the high-strain variant is stiffer and more viscous than the WT one.

Mechanochemical determinants of enzymatic activity

After ascertaining that the high-strain mutants display a different viscoelastic response than those in the control group, we tested for the effect on enzymatic activity. This was measured using a fluorescence assay of the phosphorylation of GMP to guanosine diphosphate (GDP). Figure 5a summarizes the activity for each mutant, grouped by the location of mutation. Most evident is the effect of mutation to evolutionarily conserved (Supplementary Fig. 5) residues directly involved in binding to the substrate or co-factor (binding)[95] in which, perhaps unsurprisingly, single amino acid replacements disrupted the enzymatic activity almost completely; all mutations in this group reduced the activity to below 50% of the cysteine-substituted WT* activity. We also observe significant activity disruption for mutations in the high-strain region; 9 out of 11 of these mutations exhibited reduced activity below 50% of WT* activity. By contrast, only 2 out of 14 mutations in the control region had such an effect on enzymatic activity; the most noticable of these, I118F, is the only mutant with a large predicted effect on stability, $\Delta\Delta G$ (Supplementary Fig. 6). The activity differences between the groups are significant for the high-strain and control groups (two-sided t-test, $P = 0.002$, $n = 25$) but not between the high-strain and binding groups (two-sided t-test, $P = 0.26$, $n = 20$).

The arrangement of amino acids at the binding sites is essential to protein function. Fittingly, substitutions at these locations were found to strongly reduce the catalytic activity. However, substitutions located far from the binding sites may also affect activity[27,28,69,113]. To take into account binding interactions, we primarily rely on ref. 95, determining which guanylate kinase residues are in contact with either the substrate or the metal co-factor. Because this information was limited to a few

https://doi.org/10.1038/s41567-025-02825-9

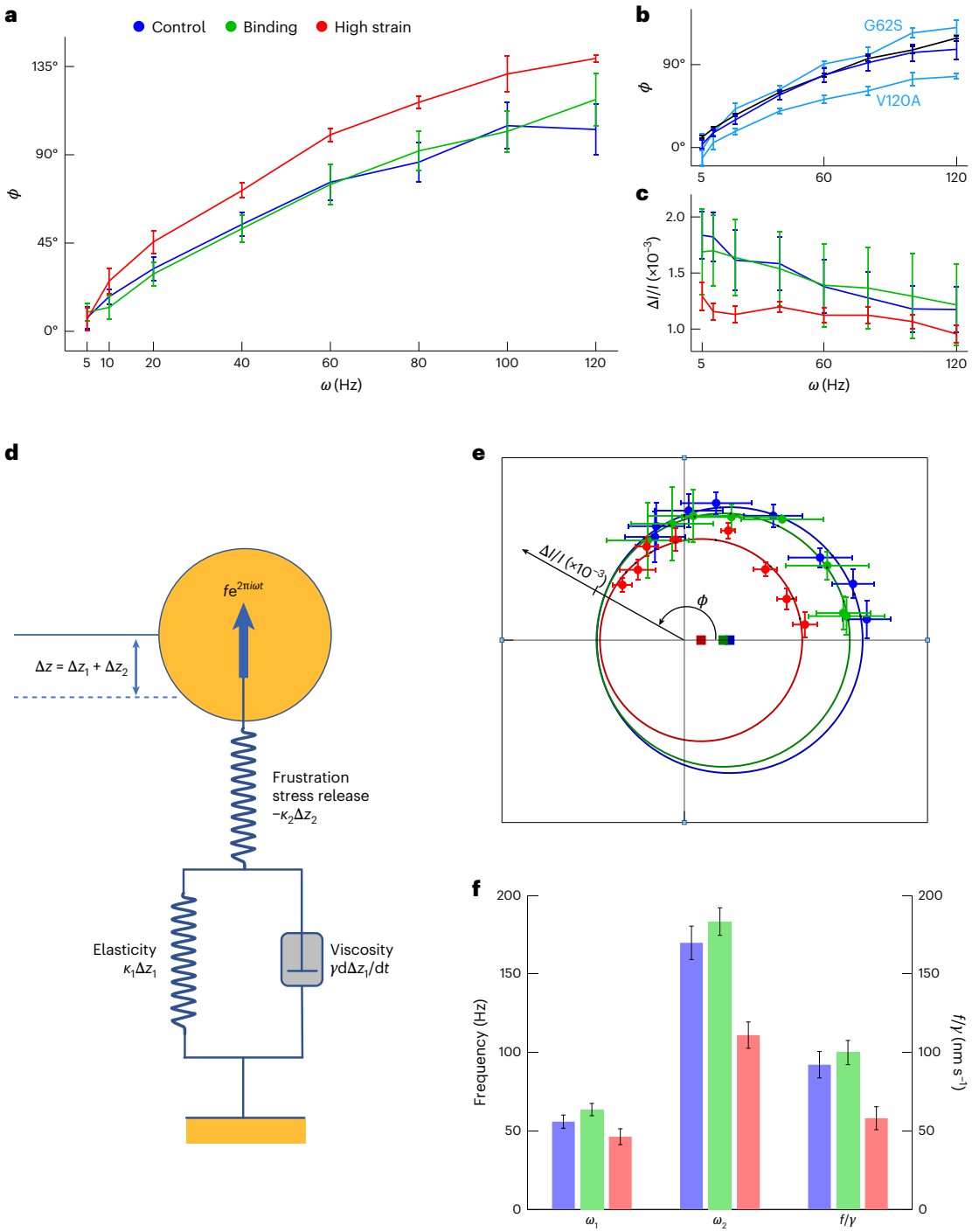

Fig. 3 | Nano-rheology experimental results and model. a, Average response phase ϕ for each mutant group as a function of frequency ω. Mutations in high-strain regions (E173N, P29V, A175T and D179S) are shown in red; control regions (G62S and V120A) and WT*, in blue; and binding-site regions (S30Q, G33S and R60K), in green. The high-strain group significantly differed from the control group ($F_{2,52} = 11.62$, $P < 10^{-4}$) and binding group ($F_{2,52} = 21.62$, $P < 10^{-6}$), whereas the binding and control groups were statistically similar ($F_{2,44} = 2.26$, $P = 0.12$) (extra-sum-of-squares F-test). The error bars show the standard error from the last averaging step (averaging of mutants into groups). Mutants per group: $N^{\text{High-Strain}} = 4$, $N^{\text{Control}} = 3$ and $N^{\text{Binding}} = 3$; total droplets measured per group: $M^{\text{High-Strain}} = 39$, $M^{\text{Control}} = 103$ and $M^{\text{Binding}} = 30$. **b**, Average response phase ϕ for individual mutants comprising the control group. Mutants are shown in light blue; WT*, in black; and the overall group average, in dark blue. The error bars show the standard error from the second averaging step (averaging over the measurement days for each mutant). Mutants G62S and V120A are denoted. Days per mutant: $D^{\text{G62S}} = 7$, $D^{\text{V120A}} = 3$ and $D^{\text{WT*}} = 12$; total droplets measured: $M^{\text{G62S}} = 12$, $M^{\text{V120A}} = 15$ and $M^{\text{WT*}} = 76$. **c**, Average response amplitude $\Delta I/I$ for each group as a function of frequency ω. The groups and error bar calculations are the same as those in **a**. The curves for individual mutants comprising the groups in **a** and **c** are shown in Extended Data Fig. 3. **d**, Viscoelastic protein model (Methods) includes an elastic spring with spring constant κ_1, a viscous damper ('dashpot') with friction coefficient γ and a stress-release element with spring constant κ_2. The overall response of the protein to the applied oscillating force $fe^{2\pi i\omega t}$ is the sum over the extensions $\Delta z = \Delta z_1 + \Delta z_2$. **e**, Depiction in the (r, ϕ) plane. Averaging was done vectorially, where r is the response amplitude ($\Delta I/I$) and ϕ is the phase. Fits are to the circle given by the viscoelastic model, with squares marking the centre of each circle. Scale bar, $\Delta I/I = 1 \times 10^{-3}$. Groups and error bar calculations are the same as those in **a**. **f**, Values obtained from fitting the model parameters to the data shown in **e**. The error bars show the 95% confidence interval of the fit.

https://doi.org/10.1038/s41567-025-02825-9

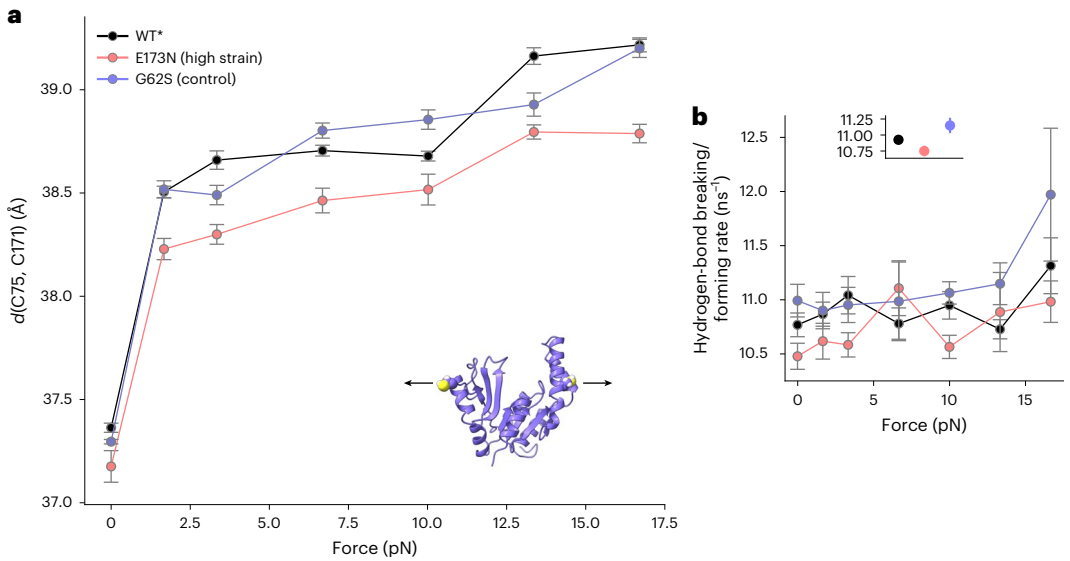

Fig. 4 | Simulation of the pulled-apart enzyme. a, MD simulations of guanylate kinase variants (WT*, E173N and G62S) pulled apart by a constant force applied between the C75 and C171 residues (inset), alongside equilibrium simulations (zero force). Mean C_α distance between C75 and C171 as a function of the strength of a constant force pulling the C75 and C171 residues apart. The error bars show the standard error ($n = 10$). **b**, Ensemble average of the rate of breaking/forming of intraprotein hydrogen bonds as a function of the pulling force. The inset indicates the average values over all the simulations (the error bars show the standard error; $n = 70$).

residues, we additionally calculated the C_α distance from GDP, ADP and Mg using an equilibrated structure (obtained from O. Delalande, S. Sacquin-More and M. Baaden (personal communication)). The minimum distance to either substrate is shown in Extended Data Fig. 6. The impact of the control mutants on activity appears to be independent of distance from the binding site (Fig. 5b; Pearson's $r = -0.19$, $P = 0.51$, $n = 14$), whereas the high-strain mutants have stronger effects closer to the binding site (Fig. 5b; Pearson's $r = -0.75$, $P = 0.008$, $n = 11$).

Enzyme function depends not only on short-ranged binding but also on large-scale protein structure and dynamics[21,50,52,114–117]. In line with that, we find a negative correlation (Pearson's $r = -0.63$, $P = 0.001$, $n = 25$) between the binding strain and enzymatic activity (Fig. 5c), which is independent of the strain threshold of 0.04 that we used to identify high-strain mutants. Furthermore, we show that mutation strain, which is measured by comparing the WT* and mutant structures predicted by AF (Fig. 5d), is also negatively correlated (Pearson's $r = -0.42$, $P = 0.043$, $n = 25$) with enzymatic activity; larger structural changes are more likely to disrupt activity. In Fig. 5c,d, we exclude the binding residues because they would impact function due to chemical changes, regardless of how they affect the structure. Yet we still see significant correlations if they are included (binding strain, Pearson's $r = 0.52$, $P = 0.002$; mutation strain, $r = 0.35$, $P = 0.046$; $n = 34$; Supplementary Fig. 7).

Discussion

We have inspected the impact of single amino acid replacements in the guanylate kinase enzyme, at three classes of functionally different locations of the enzyme, characterized into high-strain, binding and control (low-strain, non-binding) groups. We found evidence of location-dependent changes, evident in both mechanical compliance measured via nano-rheological response and in enzymatic activity.

Theory[57,58,68] explains the evolution of the high-strain region as a functional unit and shows that, to some degree, the amino acid sequences that make up these regions co-evolve towards a phenotypic trait exhibiting high strain during conformational change. Thus, even a single change in a high-strain region may affect the collective mechanical response of the protein. Our measurements indeed show that single amino acid replacements within the high-strain region significantly impact the viscoelasticity of the protein. We did not observe such an effect with mutations in the binding-site or control regions. This confirms that the high-strain region uniquely determines a substantial part of the viscoelastic behaviour. Results from nano-rheology experiments (Fig. 3) and MD simulations (Fig. 4) show a reduced amplitude of motion for mutants in this group, indicating that the WT high-strain region is more flexible and less viscous.

A model of the enzyme as a Kelvin–Voigt element[118,119] enhanced with additional prestress[55], does a very good job at describing the experimental data. The inclusion of prestress is sensible given the constraints of a folded protein, where many bonds cannot be relaxed to their minimal energy configuration due to frustration[100]. It naturally explains the extension of the phase measurements beyond 90°, which cannot happen with only one spring and one dashpot.

Fitting the averaged group data to the model quantitatively shows the stiffening of the protein when amino acids along the high-strain areas are mutated. The averaged effective viscosity γ increased by 60%, whereas the averaged spring constants for the viscoelastic response and the stress release κ_1 and κ_2 increased by 20% and 50%, respectively. Note that these values represent the averaged viscoelastic behaviour of each group, whereas the impact of specific amino acid substitutions on the behaviour of individual mutants varies.

The enzymatic activity assay (Fig. 5) examines the effect of single amino acid replacements on aspects other than the viscoelastic behaviour. Replacements in the binding region consistently reduced activity, presumably due to inflicted changes in aspects of the binding and catalysis processes. More impressive, perhaps, is the observation that mutations in the high-strain region locations are also correlated with a reduction in activity. Strain due to binding (estimated from the PDB) and strain due to mutation (estimated by AF) both correlate with activity, indicating that these independent quantitative theoretical measures of local deformation due to binding and mutation are important characteristics of the enzyme. Curiously, we found a few mutations that increased activity; following the general assumption that enzymes are adapted through evolution, we suspect that these mutations may simultaneously reduce specificity. This is consistent with a competitive activity assay we ran on five of the mutants, using adenosine monophosphate as a competitor for the native substrate

https://doi.org/10.1038/s41567-025-02825-9

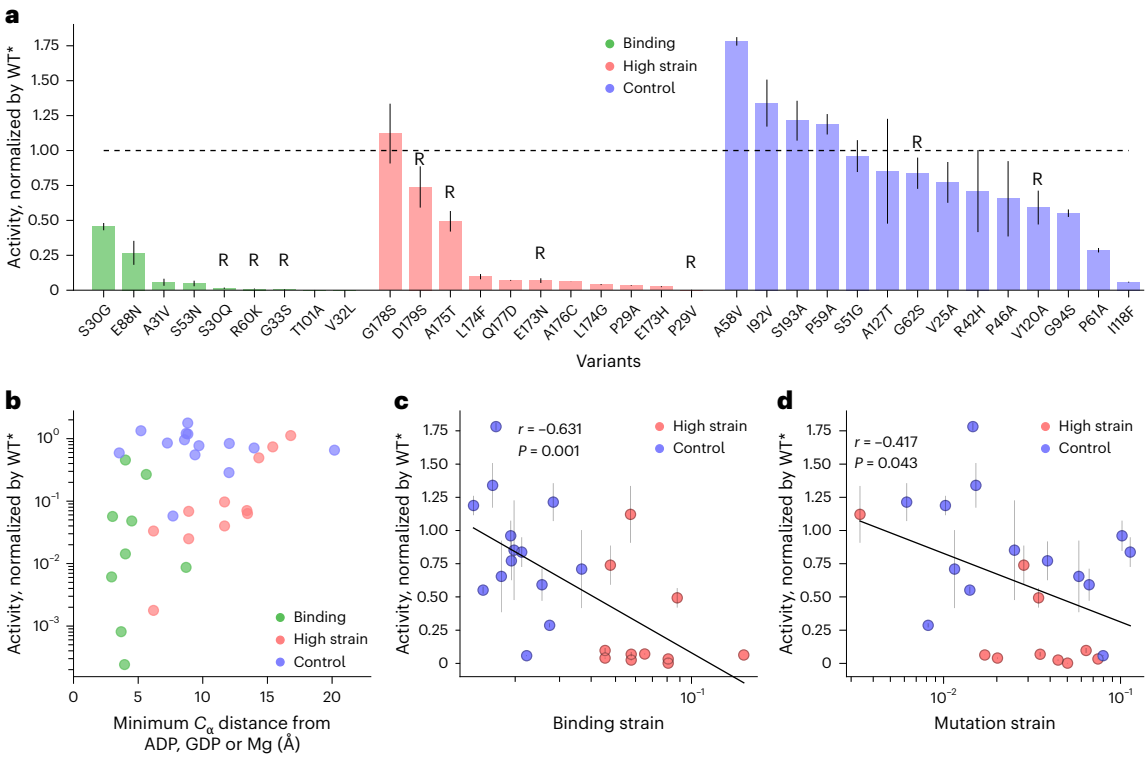

Fig. 5 | Enzymatic activity measurements. a, Enzymatic activity for each mutant as measured using a fluorescence assay of the phosphorylation of GMP to GDP. Activity was normalized by the activity of the WT* enzyme. Mutants are labelled as one of three groups: binding, if the mutated residue is in contact with a substrate or a co-factor[95]; high strain, for residues far from the binding sites that have a strain of >0.04; all other mutants are labelled control. The R letters indicate mutants studied in the nano-rheology experiments. The number of measurements averaged for each mutant is detailed in Extended Data Table 1. Individual data points are shown in Extended Data Fig. 5. Statistical differences between groups (two-sided *t*-test): control–binding, $P = 0.0001$, $n = 23$; control–high strain, $P = 0.002$, $n = 25$; high strain–binding, $P = 0.26$, $n = 20$. **b**, Activity versus the minimum distance to GDP, ADP or Mg; residues are highlighted with colour according to their group. **c**, Enzymatic activity as a function of binding strain (Methods), measured at the mutated site, for all except the binding-group mutants; the black line shows the linear fit. Pearson's correlation coefficient and *P* value are displayed on the graph ($n = 25$). **d**, Enzymatic activity as a function of strain due to mutation, measured at the mutated site, for all except the binding-group mutants; the black line shows the linear fit. Pearson's correlation coefficient and *P* value are displayed on the graph ($n = 25$). The error bars show the mean ± standard error.

GMP (Supplementary Text 1), showing reduced specificity compared with the WT enzyme.

In perspective, our results are highly consistent with the theoretical explanation of the evolution of a high-strain region and the expected effect of single amino acid mutations in it. It confirms our main hypothesis that high-strain regions play an important role in determining the enzyme's function.

Limitations and future work

Our findings differ in several aspects from previous reports on viscoelastic behaviour[120]. First, the phase–frequency curve $\phi(\omega)$ we observe (Fig. 3a) reflects the parallel actions of elasticity and viscosity (Kelvin–Voigt model[118,119]), whereas a previous measurement suggests action in series (Maxwell model[121]). Second, the phase shift measured at the highest frequencies can attain values larger than 90°. This behaviour is beyond the simple Maxwell or Kelvin–Voigt models, and indicates the participation of additional internal degrees of freedom. Our measurements are consistent with the idea that this additional physical component is stress released from preconstrained bonds[55] in the geometrically frustrated amino acid networks of proteins[100,122].

The measurement of activity using the enzymatic assay typically yields a mixture of information on the enzymatic rate constant k_{cat} and the Michaelis constant K_M. It is, therefore, possible that the change in flexibility for some mutants affects the binding, either to GMP/GDP or to ATP/ADP[45,50,83,102,123,124]. By contrast, it could be that the mechanics affects the catalytic rate k_{cat}, and that binding is not impaired, although theories linking k_{cat} to protein dynamics are less well supported[51,53,83,90,125,126]. Indeed, future work measuring the dissociation constant K_D (or K_M) for both GMP and ATP, and for all 34 mutants, could help resolve the relative contribution of changes in k_{cat} versus K_D to decreased functionality.

The question of an appropriate sample size is always relevant in an experimental setting, and there are two ways to expand on our results. First, we could investigate more enzymes, perhaps those with even better characterized and larger changes during binding. Indeed, in ref. 62, we analyse a large number of mutations in three other proteins and relate the strain at the site of mutation to enzyme functionality. However, here we focus on how the large-scale viscoelastic response of high-strain substitutions differs from that of the WT and control substitutions. Given that the nano-rheological experiments are time-consuming, the expansion of experiments to other enzymes is a goal of future work. Second, we could add more mutations to the existing guanylate kinase work. Our experimental measurement of enzymatic activity already exhibits very strong statistical significance (Fig. 5); therefore, enlarging the sample size is unlikely to alter our conclusions. By contrast, nano-rheology is a more demanding experiment, and the sample size is accordingly smaller. We expect that for these direct measurements of viscoelasticity, future work that will average over more mutants can improve on the (already significant) statistical result and arrive at a more precise estimate of the effect size. In both cases, we do not foresee a change in any of our conclusions with the growth in sample size.

The choice of the enzyme guanylate kinase from *M. tuberculosis* is mainly based on the possibility of comparing with previous results[120].

This enzyme belongs to a large class of proteins whose function involves conformational changes[19,38,39,45,50,71,83,96,97]. Although one generally expects that a protein that does not move much during function will be less influenced by mechanical perturbations, even moderate motions have been shown to be functionally relevant[35,127,128]. Such mechanical effects may be examined and generalized in future studies using the present combined methodology of identifying high-strain residues and then probing the effects of mutations by measuring tandem nano-rheology and chemical activity. Our imperfect procedure of selecting mutations (Methods) was satisfactory in exhibiting a broad range of mechanical and chemical effects, which allowed us to examine the main hypothesis. However, it was clear that the noise and uncertainty in our results could be considerably improved by future studies with larger sets of systematically chosen mutations in additional proteins.

Our viscoelastic model complements and advances beyond the standard treatment of proteins in terms of elastic networks[19,46,49,57,58,68,74,76,85,86], which are particularly useful in analysing the motions involved in binding[34]. The effective viscous forces describe the internal friction due to the breaking and reforming intramolecular bonds, the resulting local rearrangement and the interactions with surrounding water and ions. The interplay of friction and elasticity yields typical timescales for the motion (such as frequencies ω_1 and ω_2), which are absent from standard elastic network models. A natural future step will be the extension of our continuum model by formulating a viscoelastic network model that accounts for the dynamics and changing topology of the amino acid bond network.

Conclusions

On the basis of previous theoretical studies predicting that high-strain regions in proteins facilitate large-scale conformational change[34,57,58,68], we hypothesized that mutations in these regions would impact the mechanical properties of the enzyme guanylate kinase. We find this to be true for mutations in the high-strain region but not in the binding and control regions. Furthermore, we find that these mutations also greatly restrict the enzymatic activity, strongly suggesting that mechanics determines function.

To test this hypothesis, we fit results from a nano-rheology experiment to a viscoelastic model that decomposes protein motion into elastic (bond stretching and relaxation of the frustrated bonds) and viscous (bond breaking and reforming/friction) components. We find that mutations in high-strain regions make guanylate kinase slower and stiffer, which we conjecture disrupts the delicate balance between open and closed conformations, thereby affecting the transition rates and ultimately impacting the enzyme function. The characteristic mechanical frequencies of guanylate kinase are on the same order as its turnover rate, suggesting that viscoelasticity limits the catalytic rates of enzymes whose function relies on large-scale motion.

Our study demonstrates that computing binding strain by comparing as few as two protein structures[66,68,78] and, independently, using a folding algorithm (AF) to predict structural changes induced by single mutations[62,64] (mutation strain) can identify amino acids critical for protein mechanics. Altogether, our findings demonstrate that proteins have evolved collective mechanical modes with high-strain deformations that facilitate their biological function. These viscoelastic modes are governed by a small number of effective parameters (spring constants, viscosities and characteristic frequencies[79,129]) that emerge from the collective physical interactions among the amino acids encoded in the gene[19,56,61,87,130]. This is an example of the entanglement of material properties, evolutionary information and biochemical function that is a hallmark of living matter.

Online content

Any methods, additional references, Nature Portfolio reporting summaries, source data, extended data, supplementary information, acknowledgements, peer review information; details of author contributions and competing interests; and statements of data and code availability are available at https://doi.org/10.1038/s41567-025-02825-9.

References

1. Warshel, A. & Levitt, M. Theoretical studies of enzymic reactions: dielectric, electrostatic and steric stabilization of the carbonium ion in the reaction of lysozyme. *J. Mol. Biol.* **103**, 227–249 (1976).
2. Vernon, C. A. The mechanisms of hydrolysis of glycosides and their relevance to enzyme-catalysed reactions. *Proc. R. Soc. Lond. B* **167**, 389–401 (1967).
3. Perutz, M. F. The structure and function of lysozyme—concluding remarks. *Proc. R. Soc. Lond. B* **167**, 448 (1967).
4. Warshel, A. Energetics of enzyme catalysis. *Proc. Natl Acad. Sci. USA* **75**, 5250–5254 (1978).
5. Cannon, W. R., Singleton, S. F. & Benkovic, S. J. A perspective on biological catalysis. *Nat. Struct. Biol.* **3**, 821–833 (1996).
6. Shan, S. & Herschlag, D. The change in hydrogen bond strength accompanying charge rearrangement: implications for enzymatic catalysis. *Proc. Natl Acad. Sci. USA* **93**, 14474–14479 (1996).
7. Warshel, A. Electrostatic origin of the catalytic power of enzymes and the role of preorganized active sites. *J. Biol. Chem.* **273**, 27035–27038 (1998).
8. Kraut, D. A., Carroll, K. S. & Herschlag, D. Challenges in enzyme mechanism and energetics. *Annu. Rev. Biochem.* **72**, 517–571 (2003).
9. Warshel, A. et al. Electrostatic basis for enzyme catalysis. *Chem. Rev.* **106**, 3210–3235 (2006).
10. Fried, S. D., Bagchi, S. & Boxer, S. G. Extreme electric fields power catalysis in the active site of ketosteroid isomerase. *Science* **346**, 1510–1514 (2014).
11. Haldane, J. B. S. *Enzymes* (Longmans, Green and Company, 1930).
12. Pauling, L. C. Molecular architecture and biological reactions. *Chem. Eng. News* **24**, 1375–1377 (1946).
13. Pauling, L. C. Chemical achievement and hope for the future. *Am. Sci.* **36**, 51–58 (1948).
14. Cannon, W. R. & Benkovic, S. J. Solvation, reorganization energy, and biological catalysis. *J. Biol. Chem.* **273**, 26257–26260 (1998).
15. Blomberg, R. et al. Precision is essential for efficient catalysis in an evolved Kemp eliminase. *Nature* **503**, 418–421 (2013).
16. Osuna, S., Jiménez-Osés, G., Noey, E. L. & Houk, K. N. Molecular dynamics explorations of active site structure in designed and evolved enzymes. *Acc. Chem. Res.* **48**, 1080–1089 (2015).
17. Radzicka, A. & Wolfenden, R. A proficient enzyme. *Science* **267**, 90–93 (1995).
18. Wolfenden, R. & Snider, M. J. The depth of chemical time and the power of enzymes as catalysts. *Acc. Chem. Res.* **34**, 938–945 (2001).
19. McBride, J. M. & Tlusty, T. The physical logic of protein machines. *J. Stat. Mech: Theory Exp.* **2024**, 024001 (2024).
20. Saleh, T. & Kalodimos, C. G. Enzymes at work are enzymes in motion. *Science* **355**, 247–248 (2017).
21. Karplus, M. & Kuriyan, J. Molecular dynamics and protein function. *Proc. Natl Acad. Sci. USA* **102**, 6679–6685 (2005).
22. Henzler-Wildman, K. & Kern, D. Dynamic personalities of proteins. *Nature* **450**, 964–972 (2007).
23. Wei, G., Xi, W., Nussinov, R. & Ma, B. Protein ensembles: how does nature harness thermodynamic fluctuations for life? The diverse functional roles of conformational ensembles in the cell. *Chem. Rev.* **116**, 6516–6551 (2016).
24. Motlagh, H. N., Wrabl, J. O., Li, J. & Hilser, V. J. The ensemble nature of allostery. *Nature* **508**, 331–339 (2014).
25. Bahar, I., Lezon, T. R., Yang, L.-W. & Eyal, E. Global dynamics of proteins: bridging between structure and function. *Annu. Rev. Biophys.* **39**, 23–42 (2010).

26. Tang, Q.-Y. & Kaneko, K. Long-range correlation in protein dynamics: confirmation by structural data and normal mode analysis. *PLoS Comput. Biol.* **16**, e1007670 (2020).
27. Boehr, D. D., Dyson, H. J. & Wright, P. E. An NMR perspective on enzyme dynamics. *Chem. Rev.* **106**, 3055–3079 (2006).
28. Bhabha, G., Biel, J. T. & Fraser, J. S. Keep on moving: discovering and perturbing the conformational dynamics of enzymes. *Acc. Chem. Res.* **48**, 423–430 (2015).
29. Boehr, D. D. et al. A distal mutation perturbs dynamic amino acid networks in dihydrofolate reductase. *Biochemistry* **52**, 4605–4619 (2013).
30. Wong, K. F., Selzer, T., Benkovic, S. J. & Hammes-Schiffer, S. Impact of distal mutations on the network of coupled motions correlated to hydride transfer in dihydrofolate reductase. *Proc. Natl Acad. Sci. USA* **102**, 6807–6812 (2005).
31. Wang, L., Tharp, S., Selzer, T., Benkovic, S. J. & Kohen, A. Effects of a distal mutation on active site chemistry. *Biochemistry* **45**, 1383–1392 (2006).
32. Wang, X. et al. D3DistalMutation: a database to explore the effect of distal mutations on enzyme activity. *J. Chem. Inf. Model.* **61**, 2499–2508 (2021).
33. Gerstein, M., Lesk, A. M. & Chothia, C. Structural mechanisms for domain movements in proteins. *Biochemistry* **33**, 6739–6749 (1994).
34. McBride, J. M., Eckmann, J.-P. & Tlusty, T. General theory of specific binding: insights from a genetic-mechano-chemical protein model. *Mol. Biol. Evol.* **39**, msac217 (2022).
35. Gutteridge, A. & Thornton, J. Conformational changes observed in enzyme crystal structures upon substrate binding. *J. Mol. Biol.* **346**, 21–28 (2005).
36. Daniel, R. M., Dunn, R. V., Finney, J. L. & Smith, J. C. The role of dynamics in enzyme activity. *Annu. Rev. Biophys. Biomol. Struct.* **32**, 69–92 (2003).
37. Austin, R. H., Beeson, K. W., Eisenstein, L., Frauenfelder, H. & Gunsalus, I. C. Dynamics of ligand binding to myoglobin. *Biochemistry* **14**, 5355–5373 (1975).
38. Koshland, D. E. Application of a theory of enzyme specificity to protein synthesis. *Proc. Natl Acad. Sci. USA* **44**, 98–104 (1958).
39. Herschlag, D. The role of induced fit and conformational changes of enzymes in specificity and catalysis. *Bioorg. Chem.* **16**, 62–96 (1988).
40. Wang, Q. et al. Protein recognition and selection through conformational and mutually induced fit. *Proc. Natl Acad. Sci. USA* **110**, 20545–20550 (2013).
41. Ma, B. & Nussinov, R. Enzyme dynamics point to stepwise conformational selection in catalysis. *Curr. Opin. Chem. Biol.* **14**, 652–659 (2010).
42. Savir, Y. & Tlusty, T. The ribosome as an optimal decoder: a lesson in molecular recognition. *Cell* **153**, 471–479 (2013).
43. Savir, Y. & Tlusty, T. RecA-mediated homology search as a nearly optimal signal detection system. *Mol. Cell* **40**, 388–396 (2010).
44. Savir, Y. & Tlusty, T. Conformational proofreading: the impact of conformational changes on the specificity of molecular recognition. *PLoS ONE* **2**, e468 (2007).
45. Papaleo, E. et al. The role of protein loops and linkers in conformational dynamics and allostery. *Chem. Rev.* **116**, 6391–6423 (2016).
46. Bahar, I., Chennubhotla, C. & Tobi, D. Intrinsic dynamics of enzymes in the unbound state and relation to allosteric regulation. *Curr. Opin. Struct. Biol.* **17**, 633–640 (2007).
47. Goodey, N. M. & Benkovic, S. J. Allosteric regulation and catalysis emerge via a common route. *Nat. Chem. Biol.* **4**, 474–482 (2008).
48. Guo, J. & Zhou, H.-X. Protein allostery and conformational dynamics. *Chem. Rev.* **116**, 6503–6515 (2016).
49. Wodak, S. J. et al. Allostery in its many disguises: from theory to applications. *Structure* **27**, 566–578 (2019).
50. Hammes-Schiffer, S. & Benkovic, S. J. Relating protein motion to catalysis. *Annu. Rev. Biochem.* **75**, 519–541 (2006).
51. Eisenmesser, E. Z. et al. Intrinsic dynamics of an enzyme underlies catalysis. *Nature* **438**, 117–121 (2005).
52. Henzler-Wildman, K. A. et al. A hierarchy of timescales in protein dynamics is linked to enzyme catalysis. *Nature* **450**, 913–916 (2007).
53. Warshel, A. & Bora, R. P. Perspective: defining and quantifying the role of dynamics in enzyme catalysis. *J. Chem. Phys.* **144**, 180901 (2016).
54. Chaikin, P. M. & Lubensky, T. C. *Principles of Condensed Matter Physics* (Cambridge Univ. Press, 1995).
55. Alexander, S. Amorphous solids: their structure, lattice dynamics and elasticity. *Phys. Rep.* **296**, 65–236 (1998).
56. Eckmann, J.-P. & Tlusty, T. Dimensional reduction in complex living systems: where, why, and how. *BioEssays* **43**, 2100062 (2021).
57. Dutta, S., Eckmann, J.-P., Libchaber, A. & Tlusty, T. Green function of correlated genes in a minimal mechanical model of protein evolution. *Proc. Natl Acad. Sci. USA* **115**, E4559–E4568 (2018).
58. Tlusty, T., Libchaber, A. & Eckmann, J.-P. Physical model of the genotype-to-phenotype map of proteins. *Phys. Rev. X* **7**, 021037 (2017).
59. May, A. & Zacharias, M. Energy minimization in low-frequency normal modes to efficiently allow for global flexibility during systematic protein–protein docking. *Proteins* **70**, 794–809 (2008).
60. Russo, C. J., Husain, K. & Murugan, A. Soft modes as a predictive framework for low dimensional biological systems across scales. *Annu. Rev. Biophys.* https://doi.org/10.1146/annurev-biophys-081624-030543 (2024).
61. Tlusty, T. Self-referring DNA and protein: a remark on physical and geometrical aspects. *Philos. Trans. R. Soc. A* **374**, 20150070 (2016).
62. McBride, J. M. et al. AlphaFold2 can predict single-mutation effects. *Phys. Rev. Lett.* **131**, 218401 (2023).
63. McBride, J. M., Koshevarnikov, A., Siek, M., Grzybowski, B. A. & Tlusty, T. Statistical survey of chemical and geometric patterns on protein surfaces as a blueprint for protein-mimicking nanoparticles. *Small Struct.* **5**, 2400086 (2024).
64. McBride, J. M. & Tlusty, T. AI-predicted protein deformation encodes energy landscape perturbation. *Phys. Rev. Lett.* **133**, 098401 (2024).
65. Flechsig, H. & Mikhailov, A. S. Simple mechanics of protein machines. *J. R. Soc. Interface* **16**, 20190244 (2019).
66. Mitchell, M. R., Tlusty, T. & Leibler, S. Strain analysis of protein structures and low dimensionality of mechanical allosteric couplings. *Proc. Natl Acad. Sci. USA* **113**, E5847–E5855 (2016).
67. Qi, G., Lee, R. & Hayward, S. A comprehensive and non-redundant database of protein domain movements. *Bioinformatics* **21**, 2832–2838 (2005).
68. Eckmann, J. P., Rougemont, J. & Tlusty, T. Colloquium: proteins: the physics of amorphous evolving matter. *Rev. Mod. Phys.* **91**, 031001 (2019).
69. Gerstein, M. et al. Domain closure in lactoferrin: two hinges produce a see-saw motion between alternative close-packed interfaces. *J. Mol. Biol.* **234**, 357–372 (1993).
70. Wriggers, W., Chakravarty, S. & Jennings, P. A. Control of protein functional dynamics by peptide linkers. *Biopolymers***80**, 736–746 (2005).
71. Kenakin, T. & Miller, L. J. Seven transmembrane receptors as shapeshifting proteins: the impact of allosteric modulation and functional selectivity on new drug discovery. *Pharmacol. Rev.* **62**, 265 (2010).

72. Dobson, C. M. Hinge-bending and folding. *Nature* **348**, 198–199 (1990).
73. Anderson, C. M., Zucker, F. H. & Steitz, T. A. Space-filling models of kinase clefts and conformation changes. *Science* **204**, 375–380 (1979).
74. Rocks, J. W. et al. Designing allostery-inspired response in mechanical networks. *Proc. Natl Acad. Sci. USA* **114**, 2520–2525 (2017).
75. Stern, M., Liu, A. J. & Balasubramanian, V. Physical effects of learning. *Phys. Rev. E* **109**, 024311 (2024).
76. Yan, L., Ravasio, R., Brito, C. & Wyart, M. Architecture and coevolution of allosteric materials. *Proc. Natl Acad. Sci. USA* **114**, 2526–2531 (2017).
77. Landau, L. D., Pitaevskii, L. P., Kosevich, A. M. & Lifshitz, E. M. *Theory of Elasticity* Vol. 7 (Elsevier, 2012).
78. Sartori, P. & Leibler, S. Evolutionary conservation of mechanical strain distributions in functional transitions of protein structures. *Phys. Rev. X* **14**, 011042 (2024).
79. Qu, H. & Zocchi, G. How enzymes work: a look through the perspective of molecular viscoelastic properties. *Phys. Rev. X* **3**, 011009 (2013).
80. Tseng, C.-Y., Wang, A. & Zocchi, G. Mechano-chemistry of the enzyme guanylate kinase. *Europhys. Lett.* **91**, 18005 (2010).
81. Wang, Y. & Zocchi, G. Elasticity of globular proteins measured from the a.c. susceptibility. *Phys. Rev. Lett.* **105**, 238104 (2010).
82. Joseph, C., Tseng, C. Y., Zocchi, G. & Tlusty, T. Asymmetric effect of mechanical stress on the forward and reverse reaction catalyzed by an enzyme. *PLoS ONE* **9**, e101442 (2014).
83. Singh, P., Abeysinghe, T. & Kohen, A. Linking protein motion to enzyme catalysis. *Molecules* **20**, 1192–1209 (2015).
84. Shaw, D. E. et al. Atomic-level characterization of the structural dynamics of proteins. *Science* **330**, 341–346 (2010).
85. Tirion, M. M. Large amplitude elastic motions in proteins from a single-parameter, atomic analysis. *Phys. Rev. Lett.* **77**, 1905–1908 (1996).
86. Flechsig, H. Design of elastic networks with evolutionary optimized long-range communication as mechanical models of allosteric proteins. *Biophys. J.* **113**, 558–571 (2017).
87. Tlusty, T. & Libchaber, A. Life sets off a cascade of machines. *Proc. Natl Acad. Sci. USA* **122**, e2418000122 (2025).
88. Otten, R. et al. Rescue of conformational dynamics in enzyme catalysis by directed evolution. *Nat. Commun.* **9**, 1314 (2018).
89. Garcia-Viloca, M., Gao, J., Karplus, M. & Truhlar, D. G. How enzymes work: analysis by modern rate theory and computer simulations. *Science* **303**, 186–195 (2004).
90. Nashine, V. C., Hammes-Schiffer, S. & Benkovic, S. J. Coupled motions in enzyme catalysis. *Curr. Opin. Chem. Biol.* **14**, 644–651 (2010).
91. Nagel, Z. D. & Klinman, J. P. A 21st century revisionist's view at a turning point in enzymology. *Nat. Chem. Biol.* **5**, 543–550 (2009).
92. Kamerlin, S. C. L. & Warshel, A. At the dawn of the 21st century: is dynamics the missing link for understanding enzyme catalysis? *Proteins* **78**, 1339–1375 (2010).
93. Jumper, J. et al. Highly accurate protein structure prediction with AlphaFold. *Nature* **596**, 583–589 (2021).
94. Sekulic, N., Shuvalova, L., Spangenberg, O., Konrad, M. & Lavie, A. Structural characterization of the closed conformation of mouse guanylate kinase. *J. Biol. Chem.* **277**, 30236–30243 (2002).
95. Delalande, O., Sacquin-Mora, S. & Baaden, M. Enzyme closure and nucleotide binding structurally lock guanylate kinase. *Biophys. J.* **101**, 1440–1449 (2011).
96. Wankowicz, S. A., de Oliveira, S. H., Hogan, D. W., van den Bedem, H. & Fraser, J. S. Ligand binding remodels protein side-chain conformational heterogeneity. *eLife* **11**, e74114 (2022).
97. Gunasekaran, K. & Nussinov, R. How different are structurally flexible and rigid binding sites? Sequence and structural features discriminating proteins that do and do not undergo conformational change upon ligand binding. *J. Mol. Biol.* **365**, 257–273 (2007).
98. Hible, G. et al. Unique GMP-binding site in *Mycobacterium tuberculosis* guanosine monophosphate kinase. *Proteins* **62**, 489–500 (2006).
99. Tang, Q.-Y. & Kaneko, K. Dynamics-evolution correspondence in protein structures. *Phys. Rev. Lett.* **127**, 098103 (2021).
100. Ferreiro, D. U., Komives, E. A. & Wolynes, P. G. Frustration in biomolecules. *Q. Rev. Biophys.* **47**, 285–363 (2014).
101. Agarwal, P. K., Billeter, S. R., Rajagopalan, P. T. R., Benkovic, S. J. & Hammes-Schiffer, S. Network of coupled promoting motions in enzyme catalysis. *Proc. Natl Acad. Sci. USA* **99**, 2794–2799 (2002).
102. Hanoian, P., Liu, C. T., Hammes-Schiffer, S. & Benkovic, S. Perspectives on electrostatics and conformational motions in enzyme catalysis. *Acc. Chem. Res.* **48**, 482–489 (2015).
103. Romero Romero, M. L. et al. Simple yet functional phosphate-loop proteins. *Proc. Natl Acad. Sci. USA* **115**, E11943–E11950 (2018).
104. Zaccai, G. How soft is a protein? A protein dynamics force constant measured by neutron scattering. *Science* **288**, 1604–1607 (2000).
105. Radmacher, M., Fritz, M., Cleveland, J. P., Walters, D. A. & Hansma, P. K. Imaging adhesion forces and elasticity of lysozyme adsorbed on mica with the atomic force microscope. *Langmuir* **10**, 3809–3814 (1994).
106. Cellmer, T., Henry, E. R., Hofrichter, J. & Eaton, W. A. Measuring internal friction of an ultrafast-folding protein. *Proc. Natl Acad. Sci. USA* **105**, 18320–18325 (2008).
107. Hagen, J. S. Solvent viscosity and friction in protein folding dynamics. *Curr. Protein Pept. Sci.* **11**, 385–395 (2010).
108. Soranno, A. et al. Quantifying internal friction in unfolded and intrinsically disordered proteins with single-molecule spectroscopy. *Proc. Natl Acad. Sci. USA* **109**, 17800–17806 (2012).
109. Chung, H. S., Piana-Agostinetti, S., Shaw, D. E. & Eaton, W. A. Structural origin of slow diffusion in protein folding. *Science* **349**, 1504–1510 (2015).
110. Rohs, R., Etchebest, C. & Lavery, R. Unraveling proteins: a molecular mechanics study. *Biophys. J.* **76**, 2760–2768 (1999).
111. Lu, H., Isralewitz, B., Krammer, A., Vogel, V. & Schulten, K. Unfolding of titin immunoglobulin domains by steered molecular dynamics simulation. *Biophys. J.* **75**, 662–671 (1998).
112. Fisher, T. E., Oberhauser, A. F., Carrion-Vazquez, M., Marszalek, P. E. & Fernandez, J. M. The study of protein mechanics with the atomic force microscope. *Trends Biochem. Sci.* **24**, 379–384 (1999).
113. Radkiewicz, J. L. & Brooks, C. L. Protein dynamics in enzymatic catalysis: exploration of dihydrofolate reductase. *J. Am. Chem. Soc.* **122**, 225–231 (2000).
114. Kozlowski, R., Zhao, J. & Dyer, R. B. Acceleration of catalysis in dihydrofolate reductase by transient, site-specific photothermal excitation. *Proc. Natl Acad. Sci. USA* **118**, e2014592118 (2021).
115. Campbell, E. et al. The role of protein dynamics in the evolution of new enzyme function. *Nat. Chem. Biol.* **12**, 944–950 (2016).
116. Palmer, A. G. Enzyme dynamics from NMR spectroscopy. *Acc. Chem. Res.* **48**, 457–465 (2015).
117. Haliloglu, T. & Bahar, I. Adaptability of protein structures to enable functional interactions and evolutionary implications. *Curr. Opin. Struct. Biol.* **35**, 17–23 (2015).
118. Thomson, W. IV. On the elasticity and viscosity of metals. *Proc. R. Soc. Lond.* **14**, 289–297 (1865).
119. Voigt, W. Ueber die innere Reibung der festen Körper, insbesondere der Krystalle. *Abh. Königl. Ges. Wiss. Göttingen* **36**, 3–48 (1890).
120. Alavi, Z. & Zocchi, G. Dissipation at the ångström scale: probing the surface and interior of an enzyme. *Phys. Rev. E* **97**, 052402 (2018).

121. Maxwell, J. C. IV. On the dynamical theory of gases. *Philos. Trans. R. Soc. Lond* **157**, 49–88 (1867).
122. Rouviere, E., Ranganathan, R. & Rivoire, O. Emergence of single- versus multi-state allostery. *PRX Life* **1**, 023004 (2023).
123. Henzler-Wildman, K. et al. Intrinsic motions along an enzymatic reaction trajectory. *Nature* **450**, 838–844 (2007).
124. Frederick, K. K., Marlow, M. S., Valentine, K. G. & Wand, A. J. Conformational entropy in molecular recognition by proteins. *Nature* **448**, 325–329 (2007).
125. Callender, R. & Dyer, R. B. The dynamical nature of enzymatic catalysis. *Acc. Chem. Res.* **48**, 407–413 (2015).
126. Schwartz, S. D. Protein dynamics and enzymatic catalysis. *J. Phys. Chem. B* **127**, 2649–2660 (2023).
127. Koshland, D. E. Conformational changes: how small is big enough? *Nat. Med.* **4**, 1112–1114 (1998).
128. Mesecar, A. D., Stoddard, B. L. & Koshland, D. E. Orbital steering in the catalytic power of enzymes: small structural changes with large catalytic consequences. *Science* **277**, 202 (1997).
129. Qu, H., Landy, J. & Zocchi, G. Cracking phase diagram for the dynamics of an enzyme. *Phys. Rev. E* **86**, 041915 (2012).
130. Savir, Y., Noor, E., Milo, R. & Tlusty, T. Cross-species analysis traces adaptation of Rubisco toward optimality in a low-dimensional landscape. *Proc. Natl Acad. Sci. USA* **107**, 3475–3480 (2010).

[1]Department of Physics of Complex Systems, Weizmann Institute of Science, Rehovot, Israel. [2]Center for Soft and Living Matter, Institute for Basic Science (IBS), Ulsan, Republic of Korea. [3]Center for Algorithmic and Robotized Synthesis, Institute for Basic Science (IBS), Ulsan, Republic of Korea. [4]Département de Physique Théorique, Université de Genève, Geneva, Switzerland. [5]Olfera, San Francisco, CA, USA. [6]Structural Proteomics Unit (SPU), Department of Life Sciences Core Facilities (LSCF), Weizmann Institute of Science, Rehovot, Israel. [7]Department of Life Sciences Core Facilities (LSCF), Weizmann Institute of Science, Rehovot, Israel. [8]Department of Biomolecular Sciences, Weizmann Institute of Science, Rehovot, Israel. [9]Department of Chemical and Structural Biology, Weizmann Institute of Science, Rehovot, Israel. [10]Institute of Organic Chemistry, Polish Academy of Sciences, Warsaw, Poland. [11]Department of Chemistry, Ulsan National Institute of Science and Technology, Ulsan, Republic of Korea. [12]Department of Physics and Astronomy, University of California, Los Angeles, CA, USA. [13]Section de Mathématiques, Université de Genève, Geneva, Switzerland. [14]Department of Physics, Ulsan National Institute of Science and Technology, Ulsan, Republic of Korea. [15]These authors contributed equally: Eyal Weinreb, John M. McBride. ✉e-mail: elisha.moses@weizmann.ac.il; tsvitlusty@gmail.com

Methods

Enzyme production and purification

We prepared 34 different mutants of the enzyme guanylate kinase from *M. tuberculosis* (Extended Data Table 1). Surface attachment to gold was enabled by cysteine replacements at locations 75 and 171 (whose axis exits the protein and traverses through the binding pocket; Fig. 2a), whereas the two existing cysteines at locations 40 and 193 of the original guanylate kinase were replaced by serines, to avoid unwanted attachment points. All the proteins produced have these substitutions; therefore, our WT, in fact, is a slightly changed enzyme that we label WT* (Extended Data Fig. 2). All the enzymes were produced using precisely the same procedure. Hence, when we report activity or nano-rheology of the WT, or compare with it, we always do so for this slightly mutated WT*. Each of these 34 mutants additionally had a single nucleic acid substitution. The 34 mutants were selected as described in the 'Selection of mutants' section.

Expression of guanylate kinase and its mutants was performed using the expression vector K151, harbouring N-terminal 14xHis-bdSumo fusion. The vector was generously obtained from D. Görlich, Max-Planck-Institute[131]. Cloning was performed by the restriction-free method[132]. Generation of guanylate kinase mutants' clones was performed by Transfer-PCR[133]. For all the guanylate kinase construct expressions, a 500-ml culture of BL21(DE3) was induced with 200-mM IPTG and grown at 15 °C overnight. The cells were harvested and lysed by sonication in a lysis buffer (20-mM Tris 7.5, 0.5-M NaCl, 1-mM DTT and 2-mM $MgCl_2$) containing 200-KU/100-ml lysozyme, 20-μg ml^{-1} DNase, 1-mM phenylmethylsulfonyl fluoride and protease inhibitor cocktail. After clarification of the mixture by centrifugation, the cleared lysate was incubated with 1-ml washed Ni beads (Adar Biotech) for 1 h at 4 °C. After removing the unbound proteins, the beads were washed three times with 50-ml lysis buffer. Guanylate kinase (without tags) was eluted from the beads following on-column cleavage with 0.1-mg bdSumo protease for 2 h at room temperature in 1-ml lysis buffer. The soup containing the cleaved guanylate kinase was removed and applied to a size exclusion column (Superdex 75 10/300, Cytiva) equilibrated with 250-mM NaCl, 50-mM Tris pH 7.5, 2-mM $MgCl_2$ and 1-mM DTT. Guanylate kinase and its mutants migrated on the size exclusion column as well as folded globular monomers. Pure monomeric guanylate kinase, migrating as a single peak at 11.5 ml was pooled, concentrated to >1 mg ml^{-1} and frozen in aliquots at −80 °C.

Selection of mutants

The procedure for selecting the positions and amino acid substitutions in the 34 mutants was as follows. First, we classified all 207 positions in guanylate kinase into three groups: binding (17 positions according to ref. 98), high strain (22 positions whose effective strain is higher than a threshold of 0.04) and control (the remaining 168 positions). We chose this threshold to delineate the tail of the strain distribution, and grouping using any threshold value from 0.024 to 0.055 results in the same conclusions. We ignore the 25 disordered positions at the N and C termini (1ZNW). Then, 30 random positions were chosen (about one-sixth of the 182 ordered positions), such that the control group is somewhat larger (14 positions) to better sample this majority group of positions, whereas the binding and high-strain groups (8 positions each) were smaller since these are minority groups in the whole protein. To avoid possible bias, the positions within each group were selected randomly, without considering other characteristics. For example, the distances from the binding site of the high-strain and control residues are random; some are distant from the binding site, whereas others are close (Fig. 5b). At 4 of the 30 positions (P29, E173, L174 (high strain) and S30 (binding)), we introduced an additional mutation to probe the landscape of possible substitutions. Thus, altogether, there are 34 substitutions: 14 in the control group, 9 in the binding group and 11 in the high-strain group.

Obviously, the precise chemical properties of the replacement amino acid could have a strong effect on the function of the enzyme[62,64]. The substitutions were, therefore, chosen to have similar physicochemical characteristics and, consequently, to be relatively less disruptive according to their BLOSUM62 scores (Extended Data Table 1). To put our selection of substitutions in context, we note that out of the 190 possible amino acid exchanges in the BLOSUM62 matrix, 144 have negative scores (76%); 25, zero (13%); and 21, positive (11%). The median score is −2 and the average score is −1.43. In comparison, most of the selected 34 exchanges have non-negative scores, with a median score of 0 and an average score of −0.09, and are, therefore, much less disruptive than average. The only two scores below −1 are −2 of P29V and −4 of L174G—both are additional mutations at these positions. Fittingly, all the purified mutants folded appropriately, as indicated by their migration in the size exclusion column as well-folded globular monomers, which is consistent with the melting temperature (T_m) measurements (Extended Data Fig. 7 and Extended Data Table 1) and $\Delta\Delta G$ predictions (Supplementary Fig. 6, where only I118F exhibits a substantial effect on stability).

The mutants chosen for the nano-rheology experiments were similarly chosen as a random subset of the 34 mutants. Although such a choice may not be optimal, it is the most likely to reduce bias. This is because there is, at present, no practical guidance from the literature on which substitution will have the maximum effect on the viscoelastic and mechanical properties of the protein.

Nano-rheology

We followed the methodology introduced earlier[79,81,120] for periodically stretching and compressing proteins; Fig. 1b shows the schematic and describes the experimental setup. Force is applied to the protein by harnessing it at two opposing amino acids to two metallic surfaces, which are then periodically pushed together and pulled apart by an alternating-current electric field. In practice, one metallic side is a nanolayer of gold deposited on a glass microscope slide, and the other side is a free, charged gold nanobead. Since the forces applied are not much larger than those associated with thermal motion, the resulting motion of the protein is slight. For a protein with the size of 5 nm, the deformation is on the order of an ångström or less.

Observing this tiny motion is made possible by a combination of optical and statistical techniques. First, the gold nanobead moves up and down in an evanescent, exponentially decaying light field created by an internally reflected laser light. This creates a very strong dependence of the intensity of light scattered by the nanobead on its distance from the surface. Second, the signal of the stimulation electric field itself is used to lock-in onto the signal from the generated motion, filtering out any motion noise created by other sources. Third, the signal is averaged both in space (over a range of millions of gold nanobeads (that is, of proteins)) and in time (over many stimulation cycles). Since the thermal motion of the nanoparticles is independent of each other, it averages to zero, whereas the driven motion is collective and survives averaging.

In detail, the guanylate kinase enzymes were attached on one side using one cysteine to a glass slide (LK Lab Korea 0302-0002) coated with 3-nm chromium followed by 30-nm gold, and attached on the other side using the second cysteine to a 20-nm gold nanosphere bead (Nanocs GP01-20-100). This produced a layer of protein-attached gold beads with centres about 15 nm above the gold surface. The coverage of gold beads within the droplet is depicted in Fig. 1c. High-resolution images of the bead coverage from two different samples are shown: one from an atomic force microscope (Bruker JPK; left) and one from a scanning electron microscope (ZEISS Ultra 55; right), indicating that the bead coverage can reach values of 500 to 1,000 beads μm^{-2}.

Gold beads were then covered with single-stranded thiol-modified DNA 32-mers (from Integrated DNA Technologies) bearing a negative charge. An evanescent field generated by a red laser light (647 nm,

from MPB Communications) emanated from the gold-covered surface, illuminating the beads, causing any small change in the vertical position of the beads to generate a change in the intensity of light scattered by them. An indium-tin-oxide-coated microscope slide with an antireflection coating on the side opposite to the indium tin oxide (Diamond Coatings) sealed the top of the sample chamber, separated from the bottom by two spacers consisting of 150-µm glass coverslips. The chamber was filled with a diluted saline sodium citrate buffer at pH 7.0 (50-mM sodium chloride and 5-mM sodium citrate; Ambion).

An alternating electric potential was applied to the top and bottom conducting boundaries of the sample to create a peak-to-peak field of about 2 V/150 µm that was able to stretch or squeeze the proteins by pulling the negatively charged gold beads. The resultant motion of the beads is detectable by the scattered light of the evanescent field. The changes in scattered light intensity, normalized by the intensity itself ($\Delta I/I$), are proportional to the change in the height of the beads from the gold surface: $\Delta I/I = \Delta z/\delta$, where δ is the characteristic length of the evanescent wave. This was shown for both blue and red laser light, with the red laser light generating additional plasmon resonance that not only enhances the signal but also complicates the simple scattering formula. The scattering occurs simultaneously from about a billion synchronized spheres, and the resolution for the average position of the beads is about a tenth of an ångström[79,81,120,129].

We deviated from the protocol in refs. 79,81,120,134 in our methods for gathering the light and processing the signal. Rather than a photodiode and a lock-in amplifier, we used a fast camera (Hamamatsu ORCA-Flash4.0) and performed a lock-in procedure in software. We also used a lower-magnification ×5 objective so that we could simultaneously image together, on a single slide, three droplets from three different enzyme mutants. Droplets were manually spotted, typically 0.5 µl per drop. We acquired the middle 256 rows of the camera's field of view, which we positioned on the centre of the droplets.

To accumulate at least six frames per oscillation period, the frame rate was gradually increased from 200 frames per second at the minimal driving frequency ω of 5 Hz to 800 frames per second at the maximum driving frequency ω of 120 Hz. Figure 1d shows an example microscopy image from which we gathered data (cropped to a single droplet). The motion of the bead is in antiphase to the voltage (Fig. 1e), due to the positive electrical potential attracting the negatively charged DNA attached to the beads, pulling them farther away from the source of the evanescence field and, thus, decreasing the amount of light scattered.

The lock-in analysis yields the amplitude of the beads' oscillation at the frequency of the driving potential and the phase difference of that oscillation from the phase of the driving potential. Figure 1d (top) depicts an example of the mean intensity during acquisition. Here the middle image shows the amplitude of the oscillations normalized by the mean intensity, whereas the bottom image shows the phase difference; both are obtained using the lock-in method. The values of the amplitude and phase differences we report in this study were obtained by first spatially averaging the intensity signal over 16 × 16 pixel blocks and then applying the lock-in method on that signal for each block and averaging over the amplitude and phase difference values obtained from each block. For the sake of visualization, in the example shown in Fig. 1d, spatial averaging is performed over 8 × 8 pixel blocks. Data were typically taken from the droplets over regions of interest that were annular in shape, reflecting the fact that the coverage is the highest at the circumference of the drop.

It was previously shown[79–81,120] that the amplitude measured in this experimental system can vary between samples, possibly due to inconsistency in preparation. For instance, we do not control for the fact that two enzymes, rather than one, may attach to a single gold bead. If this occurs, the two enzymes will act as springs connected in parallel, and the amplitude of the bead's motion will be reduced in half. We, thus, use the phase of the beads' motion to check if the groups behave differently, since the phase should be resistant to many of these effects.

Analysis and statistical evaluation of nano-rheology experiments

The large variability in the amplitude correlated, to some extent, with the sample preparation, leading us to average multiple measurements (M) of different samples of a specific mutant made over a single day as a single experiment. Multiple measurement days (D) of a mutant were then averaged, weighted by the inverse of the standard error within each day, to get the resulting phase difference and amplitude values for that mutant. In cases where a standard error was not defined due to at least one day with only one measurement, weighting was instead done by the number of measurements in each day. To get the values for each group of mutants, mutants were averaged similarly, weighted by the inverse of the standard error of each mutant across its measurement days. In cases where a standard error was not defined due to a mutant with only one measurement day, weighting was instead done by the number of days for each mutant. Calculation of the average and standard error of the phase difference was done using the CircStat toolbox[135]. For Fig. 3e, the data were averaged vectorially, according to the protocol detailed above. The error bars represent the standard errors of the mean, as obtained from the last stage of averaging.

Approximately half the spotted samples were usable (had uncompromised coverage and an appreciable response to stimulation). Out of these, we restricted our analysis to droplets whose intensity and phase were mostly homogeneous, as estimated by a visual inspection. Each usable droplet's quality was manually graded on a scale from 1 to 5. In the analysis, we include only droplets with grades of 2 and above, which allowed differentiation between the different groups and retaining 71% of the measurements.

To evaluate whether the mutant groups significantly differed, the phase difference curves of the groups were first fitted to a simple regression model and then compared using the extra-sum-of-squares F-test[136]. A second-order polynomial (constrained to pass through zero) was fitted to the phase difference values for all the mutants in a group, for the whole frequency range, using the same weights as described above. This was done first separately for each group, and then for all the mutants in each pair of groups joined together. The goodness of fit was compared between the joined and separate fits to assess whether the groups were indeed significantly different.

Parameters for the viscoelastic model (given below) were extracted for each mutant group. Fits to circles described by the amplitude r and phase ϕ were performed on the vectorially averaged polar data, yielding estimates for the model parameters ω_1, ω_2 and f/γ.

Strain evaluation and AF analysis

To measure deformation due to physical binding and evolutionary mutations, we estimate the effective strain[62]. Strain is a concept borrowed from continuum mechanics, which is defined as the physical deformation, or spatial derivative of displacement, in response to stress (or force). In a protein, strain is the average displacement of neighbours relative to their initial distance, and is highly correlated with the un-normalized form of the local distance difference test, namely, the local distance difference[62,64]. Mathematically, it is very similar to the frame-aligned point error, which was used in the loss function of AF[93]. Force can be random (due to thermal motion) or specific (due to binding), and strain provides an estimate of the response to both these forces. Analogously, evolutionary changes can be thought of as an effective force that changes the ground state of a protein, and the response can be measured by (mutation) strain. Effective strain S_i is defined for each residue i as the average relative change in the atomic positions of its neighbours j, from a reference to the target structure:

$$S_i = \left\langle \frac{|\Delta r_{ij}|}{|r_{ij}|} \right\rangle = \frac{1}{n_i} \sum_{j \in N_i} \frac{|r_{ij} - r'_{ij}|}{|r_{ij}|},$$

where r_{ij} is the distance between C_α positions of neighbour j to residue i in a reference structure; N_i is the set of neighbours j, defined as residues

with C_α positions within 11 Å of residue i, or $|r_{ij}| < 11$ Å; the number of neighbours is $n_i = |N_i|$; and r'_{ij} is the corresponding neighbour distance vector in a target structure that has been rotated using the Kabsch algorithm[137] to maximize overlap with r_{ij}.

In this work, we use a method that has been shown to reduce the contribution of random fluctuations to strain, as the contributions of non-stochastic forces are preserved[62,64]. We take multiple structures that differ due to random fluctuations (for example, we combine multiple versions of apo guanylate kinase). For each residue, we get $3 \times n_i$ neighbourhood tensors (for each structure), and create an average neighbourhood tensor by rotating all the neighbourhoods to a reference neighbourhood and taking the mean. Supplementary Fig. 8 shows that this method results in lower strain in specific regions in the protein, and the resulting strain is less strongly correlated with the *B*-factor (a measure of disorder in the protein crystal). Supplementary Fig. 9 shows that the results are not very sensitive to the choice of the neighbourhood cut-off radius.

We used all the available structures of WT *M. tuberculosis* guanylate kinase deposited in the PDB to calculate the strain in response to binding to GDP. There are two apo structures (1S4Q and 1ZNW) and two holo structures bound to GDP (1ZNY and 1ZNZ); we omitted one structure (1ZNX) since it contains GMP instead of GDP. We note that the WT protein sequence differs from the WT* sequence by four cysteine substitutions.

To complement this strain calculation, we also studied the following: MD predictions of apo WT and WT bound to GDP, ADP and Mg (obtained from O. Delalande, S. Sacquin-More and M. Baaden (personal communication)); AF predictions of apo WT*; and AlphaFold3 (ref. 138) predictions of WT* bound to GDP, ADP and Mg (Supplementary Text 5). Extended Data Figs. 8 and 9 show that the conclusions of the paper are robust to the choice of structures.

We predict the structures of WT* and WT* mutants using the ColabFold implementation of AF[93,139]. We run ColabFold without templates, five models, use six recycles per model, and run energy minimization using the AMBER force field to obtain the relaxed structures. For each guanylate kinase variant, we generated 5 replicate predictions for each of the 5 models, resulting in 25 structures per variant. We average over all the 25 structures when calculating the mutation strain. Averaging leads to lower strain far from the mutated sites, but not at the mutated site; thus, averaging does not affect the correlation with activity since we measure the evolutionary strain at the mutated site (Supplementary Fig. 10). All the comparisons of AF-predicted WT* and PDB structures give high template modelling scores (>0.86) for each AF model (Supplementary Fig. 11)[140], which verifies that AF-predicted WT structures closely match the experimental structures[141]. We note that, in principle, we could have used MD simulations to measure the effects of mutants on structure, but AF is faster to run by several orders of magnitude, and MD simulations are also limited by typical simulation times of microseconds.

Viscoelastic model

The forces exerted on the protein induce an internal rearrangement of the amino acids. The large-scale behaviour of these motions is treated here within a simplified coarse-grained theory: the elastic deformation, due to bonds stretched, compressed or twisted, is described as a harmonic spring with force $\kappa_1 \Delta z_1$, where κ_1 is the effective spring constant and Δz_1 is the deformation (hereafter, deformations and forces are indicated as complex numbers that include phase factors). The plastic deformation, due to breaking bonds and reforming new ones, is described as a viscous damper (a dashpot), with a friction force $\gamma \mathrm{d}\Delta z_1/\mathrm{d}t$, where γ is the effective friction coefficient and $\mathrm{d}\Delta z_1/\mathrm{d}t$ is the deformation rate. The elastic and viscous elements are connected in a parallel Kelvin–Voigt architecture (Fig. 3d). In addition, many bonds in proteins are already deformed in the equilibrium configuration due to geometrical frustration typical to a dense amorphous material[100]. Therefore, when force is exerted, such stresses may be released. Following Alexander's treatment of amorphous solids[55], this is accounted for by an effective negative force $-\kappa_2 \Delta z_2$, where Δz_2 is the deformation and κ_2 is the stress-release spring constant.

Combining the contributions from elasticity, viscosity and stress release, we find the overall deformation as a function of frequency ω, as probed by the change in nanoparticle height: $\Delta z(\omega) = \Delta z_1 + \Delta z_2 = (f/2\pi\gamma)[1/(\omega_1 + \mathrm{i}\omega) - 1/\omega_2]$. Here the oscillatory force exerted on the protein is $f\mathrm{e}^{2\pi\mathrm{i}\omega t}$, where i is the imaginary unit. The dynamics of this Kelvin–Voigt–Alexander model is determined by the characteristic velocity (f/γ) and two frequencies $\omega_1 = \kappa_1/2\pi\gamma$ (the standard relaxation frequency) and $\omega_2 = \kappa_2/2\pi\gamma$ (the 'prestress' release frequency (frustration)). In the complex plane, the deformation $\Delta z(\omega) = r\mathrm{e}^{\mathrm{i}\phi}$ is a Möbius transformation and, therefore, takes the form of a semicircle that is offset from zero along the x axis, where the amplitude of the deformation is $r = |\Delta z(\omega)|$ and the phase lag of the motion relative to the exerted force is $\phi = \arg(\Delta z(\omega))$.

Enzymatic assay

We used a nicotinamide adenine dinucleotide fluorescence enzymatic assay to measure the ATP-consuming phosphorylation of GMP to GDP performed by the guanylate kinase mutants[142]. An initial concentration of 2-mM GMP and 1-mM ATP was used. The fluorescence output was monitored over 15 min at 37 °C using a microplate reader (Tecan Infinite 200 PRO or BioTek Synergy HT). The response was fitted to a sigmoid function (initiation, linear stage and saturation), or—in the case of no saturation—to a simple linear function. The relative activity of each mutant was then estimated by the maximum slope, normalized by that of the WT enzyme. For a competitive assay, concentrations of 5 mM, 10 mM and 50 mM of the GMP competitor adenosine monophosphate were added to the enzymatic solution, and the resulting activity was normalized by the no-adenosine-monophosphate case.

MD simulations

We performed MD simulations of guanylate kinase using GROMACS (v. 2021.5). We used the AMBER ff99SB-ILDN force field for the protein and the TIP3P water model. We initialized a single protein in a dodecahedron box, with 1-nm distance between the protein and the box. We used 0.1-M concentration of Na and Cl ions, ensuring that the overall charge is zero. To get an equilibrated initial configuration, we successively performed energy minimization, a 100-ps simulation in the NVT ensemble and a 100-ps simulation in the NPT ensemble: temperature, 300 K; pressure, 1 bar. Interaction cut-offs of 1 nm are used for electrostatics. Velocity-rescale thermostat and Parrinello–Rahman barostat are used. Leapfrog integration (2-fs timestep) and Verlet neighbour lists were used.

To study the protein dynamics at zero force, we run simulations for 10×100 ns (Supplementary Fig. 2) and 3 µs (Extended Data Fig. 4 and Supplementary Figs. 3 and 4) starting from equilibrated configurations for WT*, E173N and G62S. We used the AF-predicted structures as the initial configurations, and truncated the first 18 N-terminal residues that form an unstructured tail.

PMF calculations were performed using the accelerated weight histogram method[143,144]. Calculations for the three selected mutants were performed over five repeats. Each repeat started from evenly distributed snapshots selected after 2.5 µs of the unbiased MD simulation. The PMF calculation was performed until convergence, and five PMFs, separated by 10 ns, were averaged into the reported PMF. All five repeats were similar, and Extended Data Fig. 4 shows a representative one.

Network and normal mode analyses of the protein motions from the unbiased MD simulations were performed and visualized with Bio3D[145], NetworkView[146] and ProDy[147] in interaction with VMD[148]. This analysis was performed on different 500-ns portions of the 3-µs unbiased MD simulations to ensure robustness of the results.

To study protein dynamics in response to force, we apply a constant force between residues C75 and C171 (the two residues that were mutated to cysteine in the rheology experiments), and simulations were run for 10 × 100 ns at forces ranging from 1 to 10 kJ mol^{-1} nm^{-1} (1.7 to 16.7 pN). A larger box size (2-nm distance between the protein and the box) was used for non-equilibrium simulations to avoid protein self-interactions due to partial unfolding.

Simulation trajectories are processed using GROMACS tools for further analysis: unwrapping the protein to remove breaks across periodic boundaries; translating and rotating the protein to match a reference (AF-predicted) configuration. Root-mean-square fluctuations are calculated as the variance of each residue's C_α position. Hydrogen bonds are identified using GROMACS tools.

Melting temperatures

Stability of the proteins was evaluated by measuring their melting temperatures T_m using differential scanning fluorimetry. The NanoDSF Prometheus NT.48 instrument (from NanoTemper Technologies) was used to obtain temperature-dependent fluorescence curves of tryptophan and tyrosine in response to excitation with light at 280 nm, rationing the emission at 350 nm to that at 330 nm. Capillaries with the samples were heated at a rate of 1 °C min^{-1} over the range of 20–95 °C. The melting temperatures T_m were determined as the inflection points of the melting curves, using the PR.ThermControl (v. 2.1.1) software package.

Reporting summary

Further information on research design is available in the Nature Portfolio Reporting Summary linked to this article.

Data availability

Data for nano-rheology and enzymatic activity experiments are available in Supplementary Data. Additional data are available from the corresponding authors upon request.

Code availability

Code used to calculate the strain is available via GitHub at https://github.com/mirabdi/PDAnalysis.

References

131. Frey, S. & Görlich, D. A new set of highly efficient, tag-cleaving proteases for purifying recombinant proteins. *J. Chromatogr. A* **1337**, 95–105 (2014).
132. Unger, T., Jacobovitch, Y., Dantes, A., Bernheim, R. & Peleg, Y. Applications of the Restriction Free (RF) cloning procedure for molecular manipulations and protein expression. *J. Struct. Biol.* **172**, 34–44 (2010).
133. Erijman, A., Dantes, A., Bernheim, R., Shifman, J. M. & Peleg, Y. Transfer-PCR (TPCR): a highway for DNA cloning and protein engineering. *J. Struct. Biol.* **175**, 171–177 (2011).
134. Alavi, Z., Ariyaratne, A. & Zocchi, G. Nano-rheology measurements reveal that the hydration layer of enzymes partially controls conformational dynamics. *Appl. Phys. Lett.* **106**, 203702 (2015).
135. Berens, P. CircStat: a MATLAB toolbox for circular statistics. *J. Stat. Softw.* **31**, 1–21 (2009).
136. Motulsky, H. J. *Prism 5 Statistics Guide* (GraphPad Software, 2007); https://www.graphpad.com/
137. Kabsch, W. A solution for the best rotation to relate two sets of vectors. *Acta Cryst.* **A32**, 922–923 (1976).
138. Abramson, J. et al. Accurate structure prediction of biomolecular interactions with AlphaFold 3. *Nature* **630**, 493–500 (2024).
139. Mirdita, M. et al. ColabFold: making protein folding accessible to all. *Nat. Methods* **19**, 679–682 (2022).
140. Zhang, Y. & Skolnick, J. Scoring function for automated assessment of protein structure template quality. *Proteins* **57**, 702–710 (2004).
141. Xu, J. & Zhang, Y. How significant is a protein structure similarity with TM-score=0.5? *Bioinformatics* **26**, 889–895 (2010).
142. Agarwal, K. C., Miech, R. P. & Parks, R. E. Guanylate kinases from human erythrocytes, hog brain, and rat liver. *Methods Enzymol.* **51**, 483–490 (1978).
143. Lidmar, J. Improving the efficiency of extended ensemble simulations: the accelerated weight histogram method. *Phys. Rev. E* **85**, 056708 (2012).
144. Lindahl, V., Lidmar, J. & Hess, B. Accelerated weight histogram method for exploring free energy landscapes. *J. Chem. Phys.* **141**, 044110 (2014).
145. Skjærven, L., Yao, X.-Q., Scarabelli, G. & Grant, B. J. Integrating protein structural dynamics and evolutionary analysis with Bio3D. *BMC Bioinf.* **15**, 399 (2014).
146. Sethi, A., Eargle, J., Black, A. A. & Luthey-Schulten, Z. Dynamical networks in tRNA:protein complexes. *Proc. Natl Acad. Sci. USA* **106**, 6620–6625 (2009).
147. Bakan, A., Meireles, L. M. & Bahar, I. ProDy: protein dynamics inferred from theory and experiments. *Bioinformatics* **27**, 1575–1577 (2011).
148. Humphrey, W., Dalke, A. & Schulten, K. VMD: visual molecular dynamics. *J. Mol. Graph.* **14**, 33–38 (1996).
149. Goddard, T. D. et al. UCSF ChimeraX: meeting modern challenges in visualization and analysis. *Protein Sci.* https://doi.org/10.1002/pro.3235 (2018).

Acknowledgements

This work was supported by the Institute for Basic Science, Project Code IBS-R020-D1. E.M. and E.W. were supported in part by the Israel Science Foundation (grant no. 2767/20) and the Minerva Stiftung, Germany. J.-P.E. was partially supported by the Fonds National Suisse Swissmap. S.L.'s research is funded by M. de Botton and the Jacqueline and Marc Leland Foundation. We thank S. Sacquin-Mora and M. Baaden for providing the results of MD simulations of guanylate kinase bound to ADP, GDP and Mg.

Author contributions

E.W.: conceptualization, methodology, software, formal analysis, investigation, visualization, writing (original draft). J.M.M.: methodology, software, formal analysis, investigation, visualization, writing (original draft). M.S.: methodology, investigation, visualization. J.R.: methodology, software, formal analysis. R.R.: conceptualization, methodology. Y.P.: methodology, resources, writing (original draft). T.U.: methodology, resources, writing (original draft). S.A.: methodology, resources, writing (original draft). Y.F.-S.: methodology, resources, investigation. S.L.: methodology, formal analysis, investigation, visualization. J.L.S.: methodology, resources, funding acquisition, writing (original draft). B.A.G.: supervision, resources. G.Z.: conceptualization, methodology, supervision. J.-P.E.: conceptualization, methodology, software, formal analysis, writing (original draft), supervision. E.M.: conceptualization, methodology, software, formal analysis, investigation, funding acquisition, writing (original draft), supervision. T.T.: conceptualization, methodology, software, formal analysis, funding acquisition, writing (original draft), supervision. All authors: writing (review and editing).

Competing interests

The authors declare no competing interests.

Additional information

Extended data is available for this paper at https://doi.org/10.1038/s41567-025-02825-9.

Supplementary information The online version contains supplementary material available at https://doi.org/10.1038/s41567-025-02825-9.

Correspondence and requests for materials should be addressed to Elisha Moses or Tsvi Tlusty.

Peer review information *Nature Physics* thanks Dan Thomas Major, Qian-Yuan Tang and the other, anonymous, reviewer(s) for their contribution to the peer review of this work.

https://doi.org/10.1038/s41567-025-02825-9

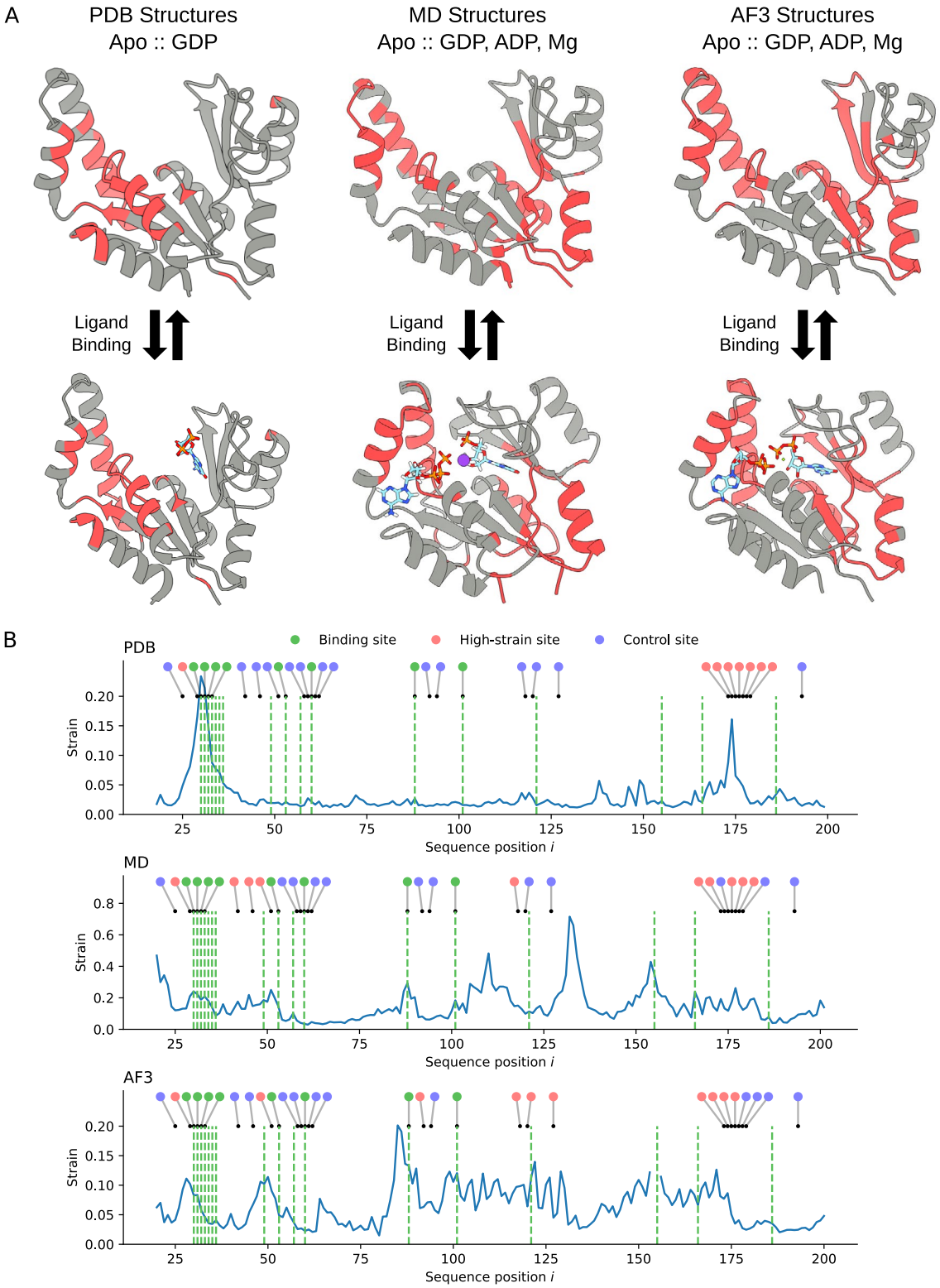

Extended Data Fig. 1 | Strain analysis of alternate guanylate kinase structures. **a** - Comparison of guanylate kinase structures before and after binding, colored by strain (residues with strain lower than median are grey, otherwise red). The same apo structure (1ZNW) is shown for all cases (differences between WT and WT* are not observable by eye). The holo structures are: **PDB** (1ZNY), WT bound to GDP; **MD**, WT bound to GDP, ADP and Mg; **AF3**, WT* bound to GDP, ADP and Mg. **b** - Strain due to binding for PDB, MD and AF3 structures (see 'Strain evaluation and AlphaFold2 (AF) Analysis' section of the Methods, and 'Alternative calculations of binding strain' section of the Supplementary Information). Locations of mutated sites for our 34 mutants are shown with black circles, with the groups indicated by colored circles; strain thresholds delineating High-Strain and Control groups are 0.04, 0.125 and 0.07.

https://doi.org/10.1038/s41567-025-02825-9

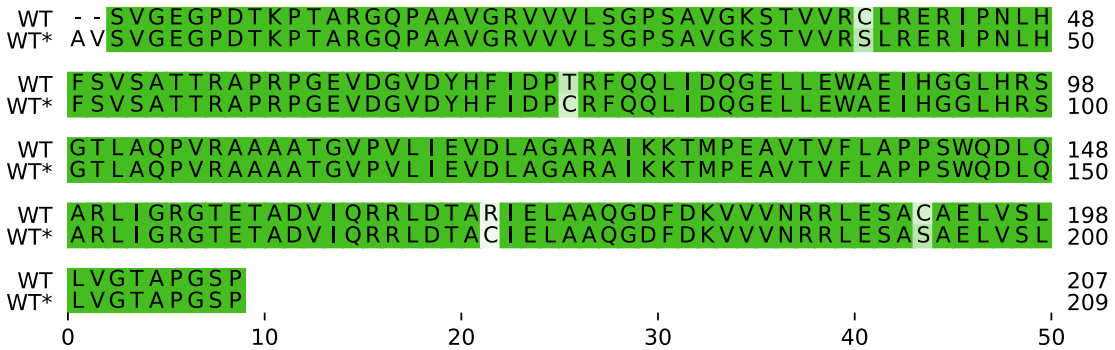

Extended Data Fig. 2 | Sequences of wild-type (WT) guanylate kinase and the cysteine-substituted variant (WT*). Sequence alignment of the wild-type (WT) sequence with the sequence of the cysteine-substituted construct (WT*) which was used as the basis of all of our experiments and the 34 variants.

https://doi.org/10.1038/s41567-025-02825-9

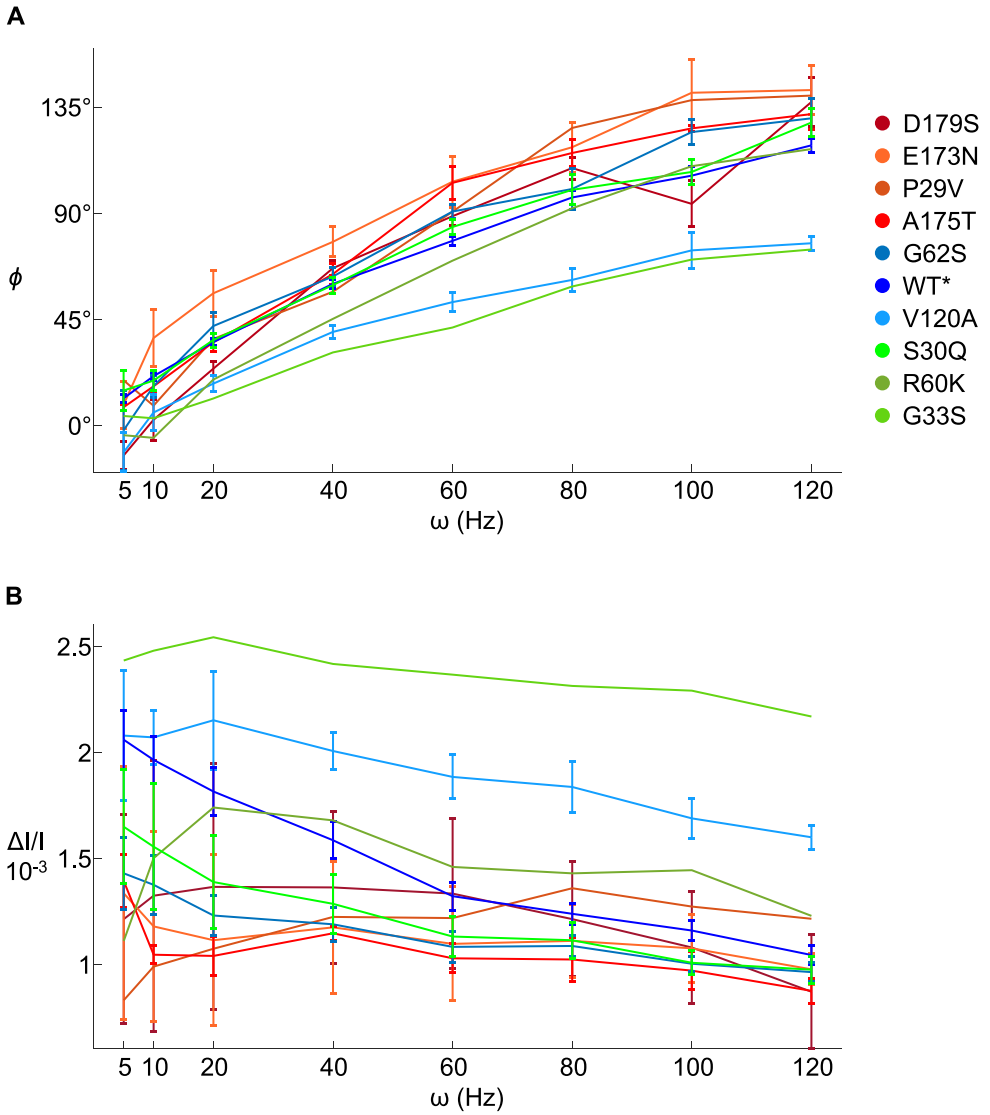

Extended Data Fig. 3 | Nano-rheology for individual mutants. Same as in Fig. 3a (**a**: phase vs frequency) and Fig. 3c (**b**: amplitude vs frequency), with curves shown for the individual mutants. Each curve represents the mean over all measurement days for an individual mutant, as specified in the Methods. Error bars show the standard error of the mean (No error bars are shown where only one measurement day was used). Mutants from the High-Strain, Control, and Binding groups are shown in reds, blues, and greens respectively. The number of measurements averaged for each mutant is detailed in Extended Data Table 1.

https://doi.org/10.1038/s41567-025-02825-9

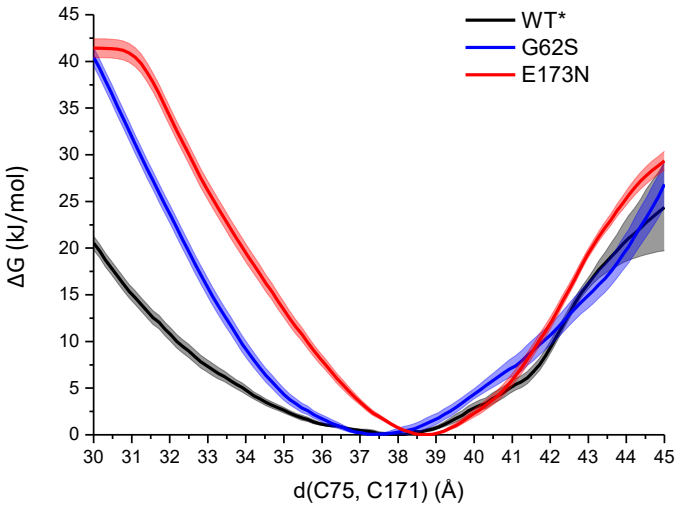

Extended Data Fig. 4 | Effective potential-of-force profiles of cysteine-cysteine distances. The potential of mean force (PMF) profiles for distance change between C75 and C171, calculated using the accelerated weight histogram method[143,144] for the wild type (WT* - black), high-strain (E173N - red), and control (G62S - blue) mutants. Standard deviation is shown shaded and is calculated for 5 slices separated by 10 ns. The spring constants κ for the different mutants can be estimated using a second order fit to the PMF curves $\Delta G = \frac{1}{2} \kappa dx^2$ for small deviations from the minimum. The resultant spring constants are 200, 260 and 500 pN/nm respectively for the WT, G62S and E173N mutants. Errors in the fits are ~10%. This is consistent with both the MD pulling simulations (Fig. 4a) and the experimentally observed stiffer response of the E173N mutant to the pulling force.

https://doi.org/10.1038/s41567-025-02825-9

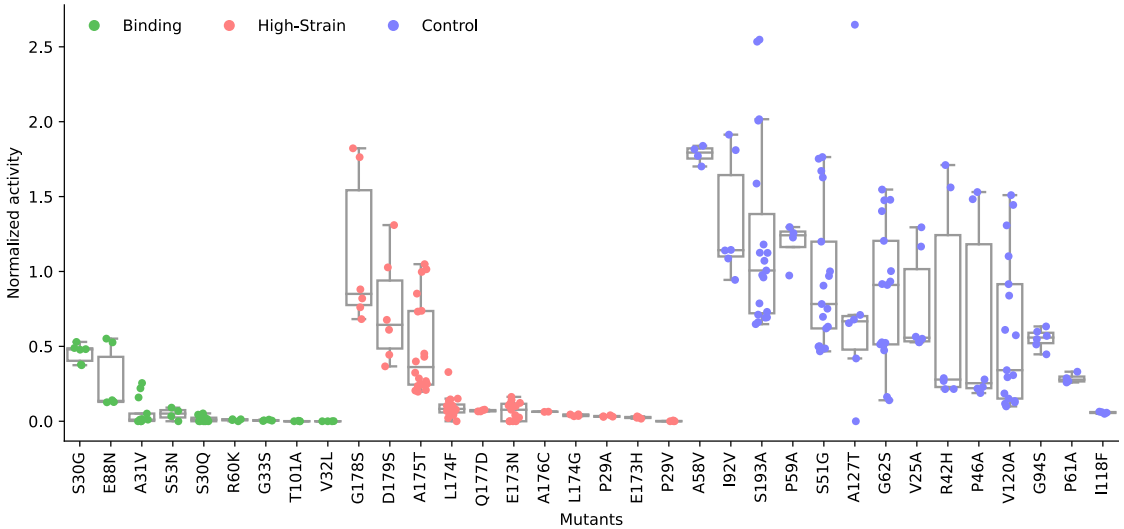

Extended Data Fig. 5 | Enzymatic activity for each mutant - with data points. Same as shown in Fig. 5a, with individual data points added. Box-plot elements: center line, median; box-limits, upper and lower quartiles; whiskers, 1.5x interquartile range or the data range, whichever is lower. The number of measurements for each mutant is detailed in Extended Data Table 1.

https://doi.org/10.1038/s41567-025-02825-9

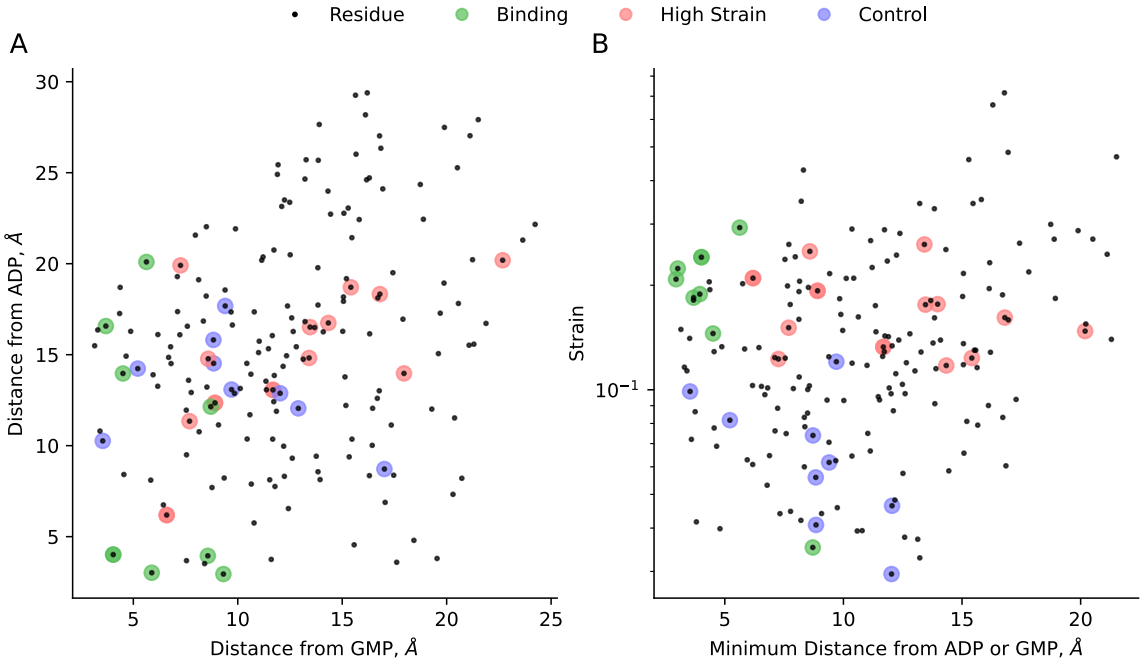

Extended Data Fig. 6 | Strain versus distance from binding sites. a - Shortest distance from each residue's C_α position to GDP versus ADP; mutated residues are highlighted, and colored by group. **b** - Strain versus the minimum distance to either GDP, ADP or Mg.

https://doi.org/10.1038/s41567-025-02825-9

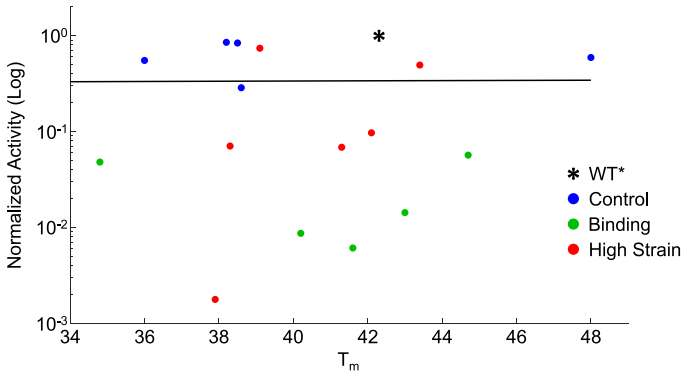

Extended Data Fig. 7 | Melting temperature T_m versus enzymatic activity. Enzymatic activity, normalized by wild type (WT*), versus melting temperature (T_m). We observe no dependence of activity on stability. Black line represents the fit to a power function. Pearson's correlation coefficient r = 0.06 p = 0.83 (n = 17). T_m values for the individual mutants are detailed in Extended Data Table 1.

https://doi.org/10.1038/s41567-025-02825-9

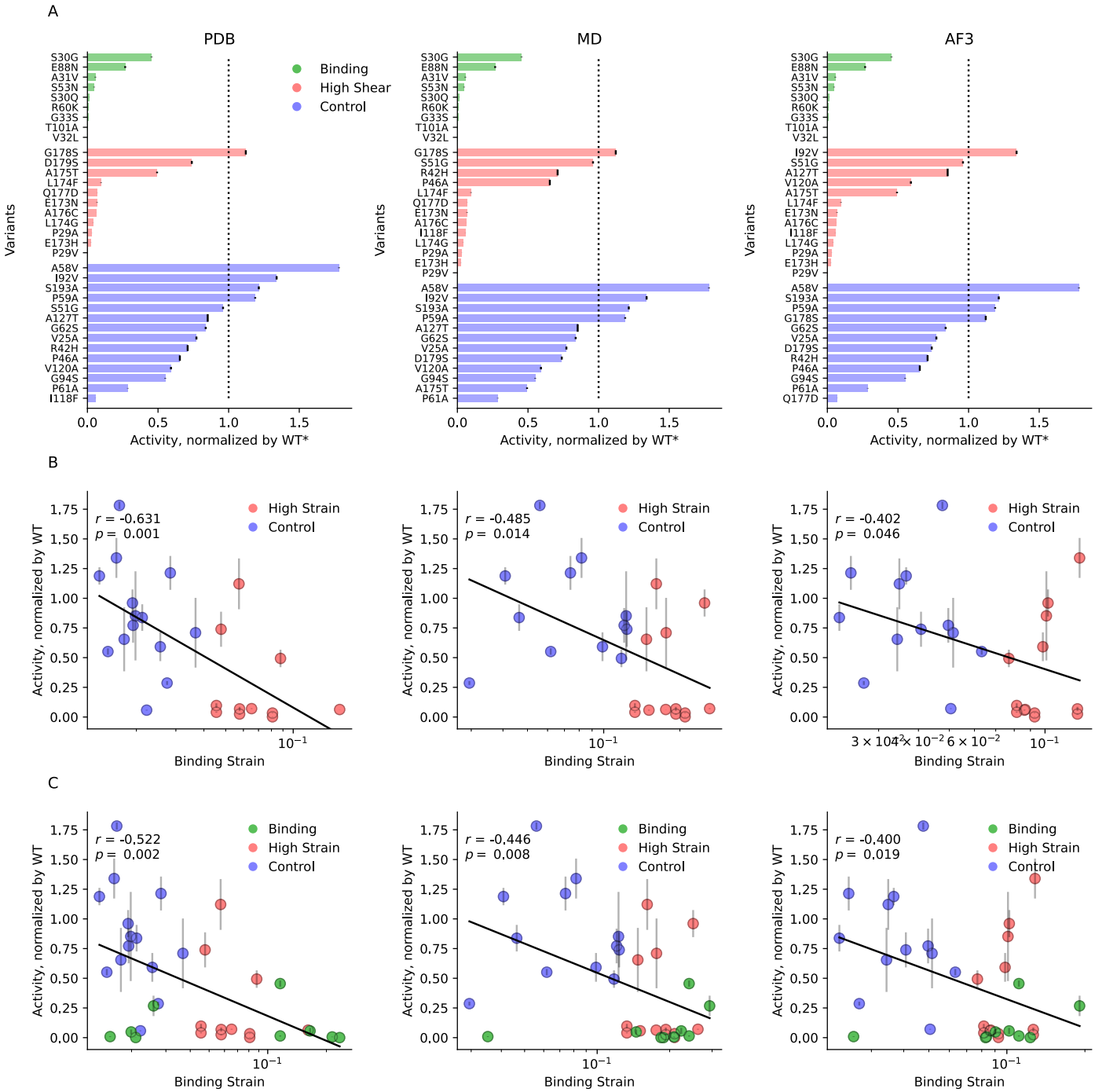

Extended Data Fig. 8 | Enzymatic activity with different strain calculations. **a** - Activity of variants, depicted according to different High-Strain / Control groupings according to different strain calculations: PDB, MD, AF3 (Extended Data Fig. 1). **b**, **c** - Strain - activity regression plots for different strain calculations, with (**b**) and without (**c**) mutants from the Binding group for PDB (**left**), MD (**middle**), and AF3 (**right**) calculations. Pearson's correlation coefficients and p-values are displayed on the graphs. Sample sizes are 25 (B) and 34 (C). The number of measurements averaged for each mutant is detailed in Extended Data Table 1. All error bars show mean ± standard error. Variants are grouped according to the thresholds given in the caption of Extended Data Fig. 1.

https://doi.org/10.1038/s41567-025-02825-9

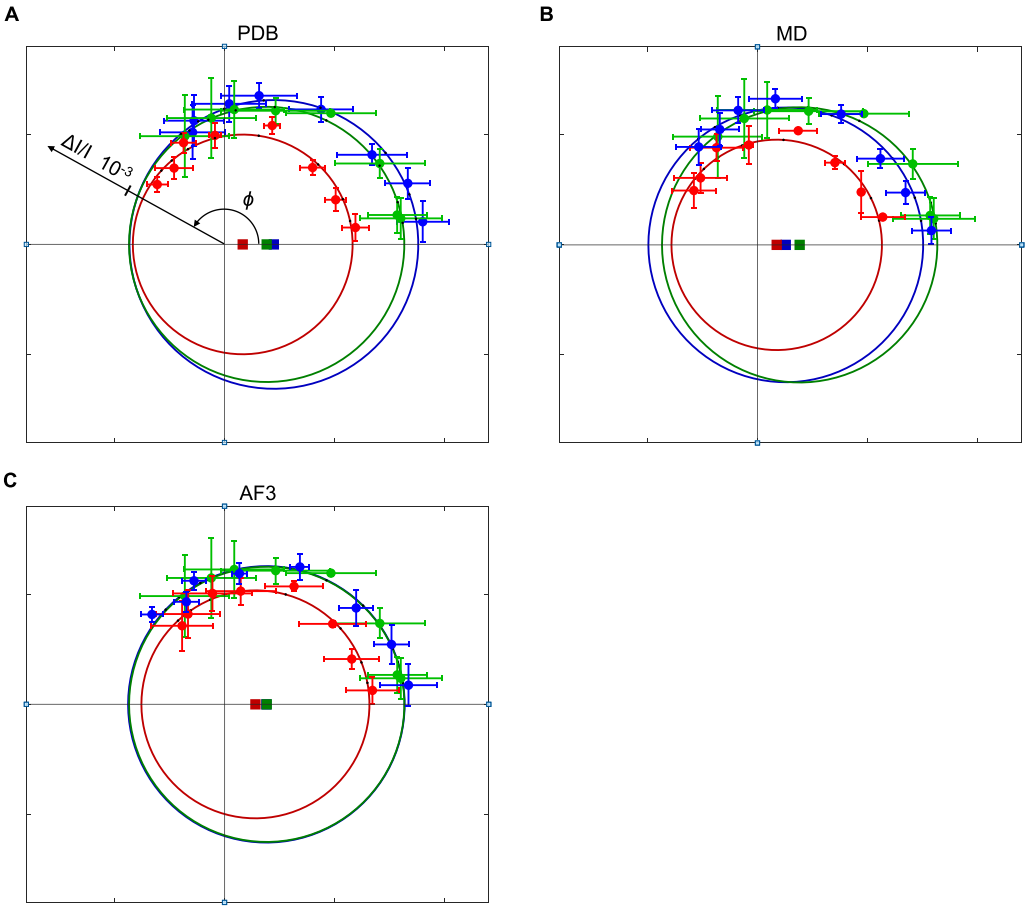

Extended Data Fig. 9 | Nano-rheology with groups chosen using different strain calculations. a–**c** - Nano-rheology amplitude-phase response, as shown in Fig. 3e, depicted according to the different High-Strain / Control groupings generated by the different strain calculations (see also Extended Data Figs. 1 and 8). Groups, sample sizes, and error bar calculations same as in Fig. 3a. Error bars show mean ± standard error.

https://doi.org/10.1038/s41567-025-02825-9

Extended Data Table 1 | Mutant details and measurements

Mutation	Group	Binding Target	Distance to GMP (Å)	Distance to ADP (Å)	Minimum Distance	Binding Strain	Mutation Strain	BLOSUM	Activity	Activity SE	Activity N	Rheology N	T_m °C	Sequence Conservation
S30G	Binding	ADP/GMP	8.24	3.34	3.34	0.097	0.02	0	0.46	0.03	6			0.65
E88N	Binding	GMP	2.64	14.86	2.64	0.026	0.01	0	0.27	0.09	6			0
A31V	Binding	ADP	10.25	2.99	2.99	0.139	0.09	0	0.06	0.03	13		44.7	0.61
S53N	Binding	GMP	2.67	12.39	2.67	0.020	0.13	1	0.05	0.02	4		34.8	0
S30Q	Binding	ADP/GMP	8.24	3.34	3.34	0.097	0.04	0	0.01	0.00	13	18	43	0.65
R60K	Binding	ADP/GMP	2.75	11.38	2.75	0.013	0.01	2	0.01	0.00	4	4	40.2	0
G33S	Binding	ADP	12.40	2.79	2.79	0.183	0.03	0	0.01	0.00	4	8	41.6	0
T101A	Binding	GMP	3.86	21.21	3.86	0.019	0.01	0	0.00	0.00	4			0
V32L	Binding	ADP	12.20	2.86	2.86	0.178	0.03	1	0.00	0.00	4			0.02
G178S	High-Strain		19.38	12.28	12.28	0.055	0.04	0	1.12	0.21	6			2.07
D179S	High-Strain		16.32	16.88	16.32	0.045	0.04	0	0.74	0.15	6	5	39.1	0.65
A175T	High-Strain		18.91	18.68	18.68	0.087	0.02	0	0.49	0.07	18	9	43.4	0.41
L174F	High-Strain		16.47	16.61	16.47	0.043	0.06	0	0.10	0.02	16		42.1	0.53
Q177D	High-Strain		17.87	16.33	16.33	0.062	0.07	0	0.07	0.00	4		38.3	1.34
E173N	High-Strain		10.51	13.53	10.51	0.056	0.05	0	0.07	0.02	13	24	41.3	0.01
A176C	High-Strain		16.50	20.47	16.50	0.164	0.03	0	0.06	0.00	2			0.28
L174G	High-Strain		16.47	16.61	16.47	0.043	0.02	-4	0.04	0.00	4			0.53
P29A	High-Strain		10.02	2.77	2.77	0.069	nan	-1	0.03	0.00	4			0
E173H	High-Strain		10.51	13.53	10.51	0.056	0.00	0	0.02	0.00	4			0.01
P29V	High-Strain		10.02	2.77	2.77	0.069	0.03	-2	0.00	0.00	4	1	37.9	0
A58V	Control		7.48	5.30	5.30	0.012	0.01	0	1.78	0.03	4			1.71
I92V	Control		3.67	14.35	3.67	0.018	0.01	3	1.34	0.17	6			1.1
S193A	Control		20.83	11.67	11.67	0.024	0.01	0	1.21	0.14	19			1.31
P59A	Control		9.35	10.16	9.35	0.011	0.11	-1	1.19	0.07	4			0.23
S51G	Control		6.65	12.00	6.65	0.017	0.01	0	0.96	0.11	17			0
A127T	Control		7.70	18.80	7.70	0.019	0.02	0	0.85	0.38	6		38.2	1.4
G62S	Control		11.67	12.98	11.67	0.014	0.06	0	0.84	0.11	17	12	38.5	0.13
V25A	Control		9.77	6.88	6.88	0.017	0.01	0	0.77	0.15	6			0.2
R42H	Control		12.54	16.62	12.54	0.033	0.07	0	0.71	0.29	6			0.31
P46A	Control		21.05	16.12	16.12	0.016	0.08	-1	0.65	0.27	6			0.4
V120A	Control		4.15	11.35	4.15	0.023	0.10	0	0.59	0.12	17	15	48	0.75
G94S	Control		9.50	14.66	9.50	0.014	0.04	0	0.55	0.03	6		36	0.76
P61A	Control		11.60	7.95	7.95	0.021	0.03	-1	0.29	0.02	4		38.6	0.09
I118F	Control		6.60	8.68	6.60	0.022	0.01	0	0.06	0.00	4			1.01
WT*											38	76	42.3	

Table of the 34 mutants used, their respective grouping, properties derived using AF, measure of strain, enzymatic activity, rheology sample sizes, T_m, and sequence conservation (measured by entropy, Supplementary Information Fig. 5; low entropy indicates a conserved position). For those in the Binding group, the binding target is also given. Entries are ordered by descending enzymatic activity within each group.